

Lineations and structural mapping of Io's paterae and mountains: Implications for internal stresses



Alexandra A. Ahern^{a,1,*}, Jani Radebaugh^a, Eric H. Christiansen^a, Ronald A. Harris^a,
E. Shannon Tass^b

^aDepartment of Geological Sciences, Brigham Young University, S389 ESC, Provo, UT, 84602, USA

^bDepartment of Statistics, Brigham Young University, 223 TMCB, Provo, UT 84602, USA

ARTICLE INFO

Article history:

Received 11 August 2016

Revised 18 May 2017

Accepted 5 June 2017

Available online 17 June 2017

ABSTRACT

The mountains of Jupiter's volcanic moon Io are tall, steep, and tectonic in origin, yet their precise modes of formation and their associations with volcanic paterae are not fully understood. Global spatial statistics of paterae and mountains and their associated lineations reveal that both types of features are more common at low latitudes and tectonic lineations have preferred orientations, whereas straight patera margins are randomly oriented. Additionally, structurally controlled lineations tend to cluster with each other, and in areas of high concentrations these tectonic lineations are shorter in length than their global average. These results indicate that global-scale (rather than local or regional) processes are involved in forming Io's tectonic structures, but that the diversity of mountain characteristics and the collapse of paterae adjacent to mountain complexes are more locally controlled. Regional structural mapping of the Hi'iaka, Shamshu, Tohil, and Zal regions reveals Io's mountains reside in large, fault-bounded crustal blocks that have undergone modification through local responses of subsurface structures to variable stresses. Strike-slip motion along reactivated faults led to the formation of transpressional and transtensional features, creating tall peaks and low basins, some of which are now occupied by paterae. We propose Io's mountains result from a combination of crustal stresses involving global and local-scale processes, dominantly volcanic loading and tidal flexing. These stresses sometimes are oriented at oblique angles to pre-existing faults, reactivating them as reverse, normal, or strike-slip faults, modifying the large, cohesive crustal blocks that many of Io's mountains reside in. Further degradation of mountains and burial of faults has occurred from extensive volcanism, mass wasting, gravitational collapse, and erosion by sublimation and sapping of sulfur-rich layers. This model of fault-bounded blocks being modified by global stresses and local structural response accounts for the variation and patterns of mountain sizes, shapes, and orientations, along with their isolation and interactions with other features. It also provides a context for the operation and extent of global and regional stresses in shaping Io's surface.

© 2017 Elsevier Inc. All rights reserved.

1. Introduction

Jupiter's moon Io, from earliest observations, has been anomalously dynamic, with a surface that is a colorful mosaic of active volcanic and tectonic features (Morabito et al., 1979; Smith et al., 1979; Strom et al., 1979; McEwen et al., 1998; McEwen et al., 2000; Spencer et al., 2007). Io's significant tidal heat (Peale et al., 1979) is released through volcanic activity (Johnson et al., 1979; Peale et al., 1979; Blaney et al., 1995; McEwen et al., 1998) and

crustal resurfacing and subsidence (Schenk and Bulmer, 1998; Schenk et al., 2001; Turtle et al., 2001; Jaeger et al., 2003). The average heat flow at the surface of Io is ~20–30 times that of Earth (O' Reilly and Davies, 1981; Veeder et al., 1994; Turcotte and Schubert, 2002; Veeder et al., 2004; Veeder et al., 2009; Veeder et al., 2011). Moreover, Io has no visible impact craters, making the surface only a few million years old (McEwen et al., 1989; Geissler et al., 1999; McEwen et al., 2000). The average resurfacing rate is ~1–10 cm/year (Johnson et al., 1979; McEwen et al., 1989), though much of this could be highly localized, with greater volumes of material emerging at volcanic centers such as lava lakes (Geissler et al., 1999; Lopes et al., 2004). The overall density, gravitational studies and topographic observations suggest that the moon's crust and mantle are primarily composed of

* Corresponding author.

E-mail address: alexandra.ahern@stonybrook.edu (A.A. Ahern).

¹ Present address: Department of Geosciences, Stony Brook University, Stony Brook, NY 11794

iron-rich silicates (McEwen et al., 1989; Carr et al., 1998; Geissler et al., 1999), but chalcophile elements, sulfur allotropes, and fresh mafic lavas give Io's surface its distinctive red, black, and yellow colors (Sagan, 1979; Carr et al., 1998; Geissler et al., 1999; Kargel et al., 1999). Many of these materials have been erupted from plumes and fissures, or onto the floors of volcanic depressions (Carr et al., 1998; Geissler et al., 1999; Lopes-Gautier et al., 1999; Davies, 2001; Radebaugh et al., 2001).

Io contains some of the tallest and steepest mountains in the solar system (Schenk et al., 2001; Turtle et al., 2001; Jaeger et al., 2003; Turtle et al., 2007), composed of mafic silicates and sulfur compounds that are thought to be Io's older and deeper crust (McEwen et al., 1998; Schenk and Bulmer, 1998). Paterae, defined on Io as volcano-tectonic depressions (Radebaugh et al., 2001), range up to over 200 km across (Radebaugh et al., 2001; Rathbun et al., 2002), and make up ~2% of the surface (Zhang et al., 2002). They resemble terrestrial calderas and often have active lava flows on their floors (Carr et al., 1998; Radebaugh et al., 2001). These tectonic and volcanic features are key to understanding crustal processes on Io and other tidally heated bodies (Carr et al., 1998; Schenk and Bulmer, 1998; Schenk et al., 2001; Turtle et al., 2001; Jaeger et al., 2003; Turtle et al., 2007).

Paterae and mountains are globally distributed (Carr et al., 1998; Radebaugh et al., 2001; Schenk et al., 2001; Jaeger et al., 2003; Kirchoff et al., 2011; Hamilton et al., 2013) and their distribution and character can provide valuable insight into volcanic and tectonic processes operating within Io's crust (Jaeger et al., 2003; Hamilton et al., 2013). The relationships of these two features to each other, as well as the processes forming them, are still not well understood (Radebaugh et al., 2001; Jaeger et al., 2003). This paper examines mountains and paterae at global and local scales through analysis of their distributions and new structural maps. This will help us begin to determine the relative influences of global and regional stresses in their formation, while also identifying how these two classes of features may be linked by tectonic interactions with one another.

2. Background

2.1. Mountains

Despite Io's persistent volcanic activity, its ~135 reported mountains (Turtle et al., 2001; Turtle et al., 2007) are, with very few exceptions, classified as tectonic rather than volcanic in origin (Schaber, 1982; Nash et al., 1986; Carr et al., 1998; Schenk et al., 2001; Turtle et al., 2001). They lack distinguishable vents, calderas, or flows emanating from their summits (Turtle et al., 2001) and are blocky and steep-sided, rather than conical. Ionian mountains have been defined by Schenk et al. (2001) as features of positive relief and measureable size higher than 1 km, not solely created by erosional processes. Schenk et al. (2001) measured the average mountain height to be 6.3 km, with Io's highest peak, Boösaule Montes, rising to 17.5 ± 3 km above the surface. They also measured the average length and width of mountains to be 158 km and 80 km, respectively, and the average area to be ~12,080 km². Mountains comprise 3% of Io's total surface area (Schenk et al., 2001).

The Voyager 1 and 2 spacecraft first observed Io's mountains up close, and studies of Voyager images suggested that the mountains were evenly distributed in both latitude and longitude and were tectonically modified crustal blocks, rather than volcanoes, as had been previously predicted (Carr et al., 1979). There was no pattern or alignment of mountains to suggest that a global tectonic regime, such as terrestrial-style plate tectonics, could be responsible for them (McEwen et al., 1989; Schenk et al., 2001; Turtle et al., 2007). Galileo's Solid State Imaging (SSI) camera imaged Io's surface from 1996–2002 (McEwen et al., 2000), further revealing the diversity

of Io's mountain morphologies, along with many smaller-scale tectonic and mass wasting features (Fig. 1) (McEwen et al., 2000).

The majority of Io's mountains appear as isolated "islands" that climb steeply out of the surrounding smooth, volcanic plains. Others have scalloped margins eroded from possible sapping of sulfur-rich crustal layers or are surrounded by debris aprons. Many bounding scarps can be interpreted as tectonic, erosional, or a result of gravitational collapse (Schenk et al., 2001), and many mountains possess lineations, striations, and troughs that could have been created by arching or detachment during uplift or by mass movement (McEwen et al., 1985; Carr et al., 1998; Schenk et al., 2001). Carr et al. (1998) and Schenk et al. (2001) compiled global catalogs of mountains from Voyager and Galileo data to better classify the variations in mountain characteristics.

Mountains are often found adjacent to paterae, leading to the conclusion that they may be genetically related (Radebaugh et al., 2001; Jaeger et al., 2003; Radebaugh, 2005). Carr et al. (1998) did not find a spatial correlation between mountains and volcanic hot spots. However, Schenk and Hargitai (1998) reported a longitudinal anticorrelation between the densest concentrations of mountains and volcanic centers, results that have since been validated in other research (McKinnon et al., 2001; Schenk et al., 2001; Kirchoff and McKinnon, 2009; Kirchoff et al., 2011). Mountains seem to be slightly more densely clustered at lower latitudes (Schenk et al., 2001) and show two broad concentrations around 65°W and 265°W, roughly antipodal from one another, 5°–25° off of the leading and trailing points of Io's orbit (McEwen and Soderblom, 1983; Schenk et al., 2001; Kirchoff et al., 2011). These concentrations are offset ~90° from two clusters of volcanic centers reported by Radebaugh et al. (2001) and Schenk et al. (2001), roughly associated with the sub- and anti-Jovian points. The global anticorrelation between mountains and volcanic centers may suggest that heat flow in the crust is higher along the Jupiter-pointing axis in the areas where volcanic centers are concentrated (Radebaugh et al., 2001), while 90° from those areas there exists colder, thicker, and more brittle crust better suited for mountain formation through thrusting or tilting of crustal blocks (Schenk and Bulmer, 1998; Schenk et al., 2001; Turtle et al., 2001; Jaeger et al., 2003; Kirchoff and McKinnon, 2009).

A number of possible formation mechanisms for Io's mountains and other tectonic features exist. McEwen et al. (1985) postulated early on that Io's crust was experiencing Basin and Range-style extension, with high heat flow below a thin lithosphere, magmatism, and topographic swelling. Keszthelyi et al. (1999) proposed that the lithosphere of Io is negatively buoyant on a dense, partially molten upper mantle and that mountains are crustal blocks associated with remixing of the lithosphere into the mantle. Others have linked diurnal tidal forces directly to the formation of smaller features. Bart et al. (2004) concluded that fields of small-scale ridges may have resulted from crustal deformation as predicted from tidal flexing, suggesting that a global input of tidal stress may overprint local stress fields. However, larger-scale structural landforms may be explained by fractures undergoing diurnal reactivation and continued slip, and non-synchronous rotation (assuming Io is rotating slightly faster than synchronous) (Bart et al., 2004). Jaeger et al. (2003) proposed that local convective upwelling due to global tidal heating may generate asthenospheric diapirs that rise and dome the surface, creating local horizontal compressive stresses outward from domes sufficient for mountain formation. Finally, because local or regional crustal temperatures are dependent on the amount of volcanism occurring in a given area (O'Reilly and Davies, 1981), an increase in the throughput of conducted heat could result in increases in crustal temperatures. McKinnon et al., (2001) and Kirchoff and McKinnon (2009) have suggested that crustal heating could generate sufficient regional compressional thermal stress to form mountains.

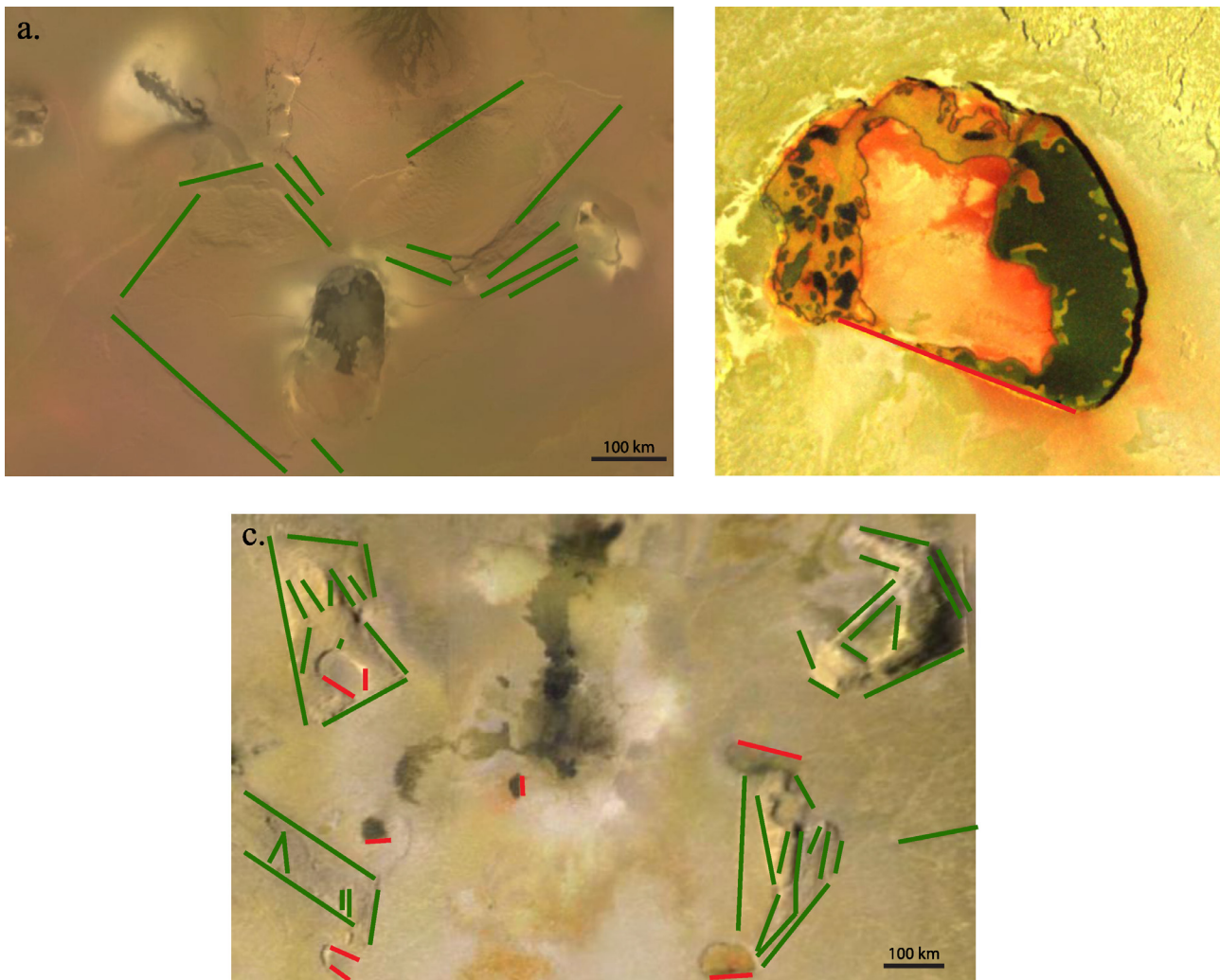


Fig. 1. Examples of lineations identified in this study. Structural lineations (green) and patera-edge lineations (red) are traced over images of (a) Euboea Montes (17.5°S, 51°W), (b) Tupa Patera (18.5°S, 141°W), and (c) the Amirani region (~25°N, 114°W). (For interpretation of the references to colour in this figure legend, the reader is referred to the web version of this article.)

Schenk and Bulmer (1998) linked horizontal shortening in the crust to vertical compressive stress generated by constant burial by volcanic deposits. They suggested Io builds successive layers of volcanic materials, causing the lithosphere to subside and thus shorten. This process develops horizontal compressive stresses that may be high enough to exceed the compressive strength of rock in the lithosphere, forcing mountain blocks to pop up along high-angle reverse faults (Schenk and Bulmer, 1998; Turtle et al., 2007; Bland and McKinnon, 2016).

2.2. Paterae

Volcanic centers on Io exist in the forms of single vents, fracture vents, flow fields, and shield volcanoes, but the majority are paterae (Lopes and Williams, 2005; Williams and Howell, 2007). Paterae are widely distributed and number over 400 (Carr et al. 1979; Radebaugh et al., 2001; Barth and Radebaugh, 2010; Williams et al., 2012). Often compared to terrestrial calderas, these depressions are attributed to collapse into a partially drained magma chamber or into voids left by the sublimation of layers of sulfur-based frosts within the crust (Radebaugh et al., 2001; Keszthelyi et al., 2004). Paterae have steep walls and flat floors that are often covered or partially covered by relatively young lava flow deposits (Radebaugh et al., 2001; Williams et al., 2012). The average patera effective diameter (diameter of a circle having the

same area as the patera) from a database of 417 paterae is 41 km (Radebaugh et al., 2001).

Hamilton et al. (2013) reported that paterae tend to be uniformly distributed in regions of more active volcanism and are more randomly distributed around Io's north pole. Radebaugh et al. (2001) found that paterae are located slightly more frequently between 25°S and 25°N latitude and cluster around 330°W and 150°W longitude (Radebaugh et al., 2001), as do all volcanic centers (Lopes-Gautier et al., 1999). These longitudinal clusters are 30–60° offset from predicted locations of maximum surface heat flux along Io's tidal axes, suggesting that magma may travel laterally by way of local subsurface conduits (Hamilton et al., 2013) rather than directly through the crust from its source. Volcanic centers, including paterae, are longitudinally anti-correlated with mountains (Schenk et al., 2001; Jaeger et al., 2003; Kirchoff et al., 2011; Hamilton et al., 2013), which has been suggested to imply that mountain and patera formation are related by global-scale processes, but that the local structural processes responsible for forming individual mountains or paterae are independent of one another (Schenk and Bulmer, 1998; McKinnon et al., 2001; Schenk et al., 2001; Kirchoff et al., 2011). While 13% of paterae are adjacent to at least one mountain, 42% of mountains have at least one adjacent patera (Radebaugh et al., 2001; Jaeger et al., 2003) indicating a probable local relationship between the two features. Kirchoff et al. (2011) also noted positive

correlations between the distributions of mountains and volcanic centers.

While terrestrial calderas are nearly always round or sub-round, many paterae have straight or angular portions to their margins (Radebaugh et al., 2001). It is possible that the straight edges of paterae, as well as their non-round shapes, indicate tectonic elements in their formation or genetic relationships to adjacent mountains.

3. Methods

We investigate possible links between mountains and paterae by analyzing spatial relationships between them and the structural features that may be related to their formation. We analyze the relationships between mountains and paterae, specifically, where previous statistical analyses examined the relationship between all volcanic centers and mountains (Carr et al., 1998; Kirchoff et al., 2011; Hamilton et al., 2013). Paterae with possible structural influence are identified and their relationships to mountains are separately characterized. Tectonic features associated with mountains are also analyzed to determine the extent of tectonic controls on mountain formation and evolution and on collapse of associated paterae using both global spatial statistics and structural mapping. This study sheds light on the processes forming mountains and paterae, sources and magnitudes of stress inputs to the crust, crustal tectonic activity, and resultant deformation.

3.1. Data

In order to investigate the extent, effects, and sources of stress in Io's crust, we have performed global spatial analyses of lineations associated with mountains and paterae. We mapped all lineations for this spatial study (Figs. 1, 2) in ArcGIS using the Io merged, north pole, and south pole mosaics as base maps under the Io 2000 Geographic Coordinate System and North Pole and South Pole projections (Williams et al., 2012). These mosaics combine Galileo color data with the high-resolution monochrome mosaic from Voyager Imaging Science Subsystem (ISS) and Galileo SSI images. The merged mosaic is a simple cylindrical map projection centered on 0° longitude, with resolution ranging from 1–10 km/pixel near the equator (lowest resolution area centered on 50° W), and no coverage within 5° of the north pole (Williams et al., 2012). Although there are resolution variations, we have mapped lineations and features for our statistics on the merged mosaic for global continuity and for ease in comparison with other work. Our data include linear features we have identified as well as databases of patera and mountain locations that we have updated (Radebaugh et al., 2001; Barth and Radebaugh, 2010).

We identified and measured lineations across the surface of Io and divided these into two categories—structural lineations and patera-edge lineations, examples of which are given in Fig. 1. Structural lineations refer to any features interpreted as faults, fractures, or folds—features that have formed as a result of tectonism (Fig. 1a). These were interpreted based on fault and fold geometries and geomorphologic characteristics of similar structures on Earth as understood from aerial photos and field studies. Patera edge lineations are defined as straight margins of paterae and have been considered alongside, but separate from, structural lineations because of their connection to paterae (Fig. 1b). These were identified anywhere a straight, rather than arcuate, segment of a patera margin exists, ranging from 2.8 km to 193 km in length (where the minimum value was not preset, but may have been determined by resolution constraints).

The azimuths and lengths of all identified lineations (Fig. 2) were calculated in ArcGIS using the COGO Toolbox. In addition to lineations, we measured the long axes of paterae and calculated

their azimuths and lengths in ArcGIS. We also measured lengths, widths, and areas in ArcGIS of 82 mountains using polygonal shapefiles to calculate areas. Of Io's ~135 mountains (Turtle et al., 2007), we were only able to discern 82 well enough to find boundaries between them and the surrounding plains at the resolutions of the global mosaic. We recognize the potential for observational biases due to lower image resolution in some locations, or to differences in viewing or illumination angles between images, but high resolution images of Io are limited. This is one reason that we selected areas of higher resolution (as explained in Section 4 of this paper) to study in greater detail—to see from both a global and local scale tectonic features that point to important processes in Io's past.

3.2. Statistical methods

We tested these data for clustering of lineations and lineation characteristics (length and azimuth) in 16 sectors of equal area across Io's surface. It is visually apparent that some features are clustered at various locations and scales (Fig. 3a), so we tested these features for spatial randomness using the *G* and *K* functions and the statistical software *R* (*R Core Team, 2015*) with the contributed “spatstat” package (Baddeley and Turner, 2005). The *G* function is a nearest neighbor distance function that quantifies spatial interaction between features. It gives the proportion of features in a set of distances up to a given cutoff, *r*, to the total number of points expected under complete spatial randomness. The *K* function is also a distance function between features but looks beyond nearest neighbors. It shows interactions between points by computing the cumulative number of features located around all others within a certain radius, *r* (Gelfand et al., 2010; Diggle, 2013). To determine the bounds for complete spatial randomness, we performed 100 runs through both the *G* and *K* functions, with randomized locations assigned to the corresponding number of features we had identified, to obtain a range in which we would reasonably expect the data to plot if they were randomly distributed. For a clustered pattern, features or measurements are closer to each other than expected from complete spatial randomness and plot above those bounds. For a uniform pattern, they are farther apart than expected and plot below the complete spatial randomness function bounds.

Additionally, we looked at the conditional marked moments, which are the conditional mean and conditional variance of the lengths and azimuths of a random lineation, given that there exists another random lineation at a distance *r* away from it. These tests are used to indicate whether similar length or azimuth values tend to cluster geographically by fixing measurement locations and varying lengths and azimuths randomly (Gelfand et al., 2010; Diggle, 2013)—in this study we ran these tests using 100 scenarios. This provides an average, with some variation for randomness, that the lengths and azimuths of our data are compared to in order to detect patterns at distances in 50 km intervals away from each feature along great circles. The number and character of each feature were analyzed along each given great circle, rather than in the cumulative area covered by all previous great circles. If points plot within the bounds of variance around the mean, then we can conclude that there is no pattern, but rather that lengths and azimuths vary randomly with location. If they plot above or below the bounds we generated, then some spatial pattern exists for the lengths or azimuths of the lineations on Io.

We used a nonparametric circular-linear correlation to correlate the azimuths and lengths of linear features since azimuth is an angular measure and length is linear. To do this, each azimuth value was converted to a ranked circular variable, β_i , by:

$$\beta_i = \frac{2\pi(r_i)}{n}$$

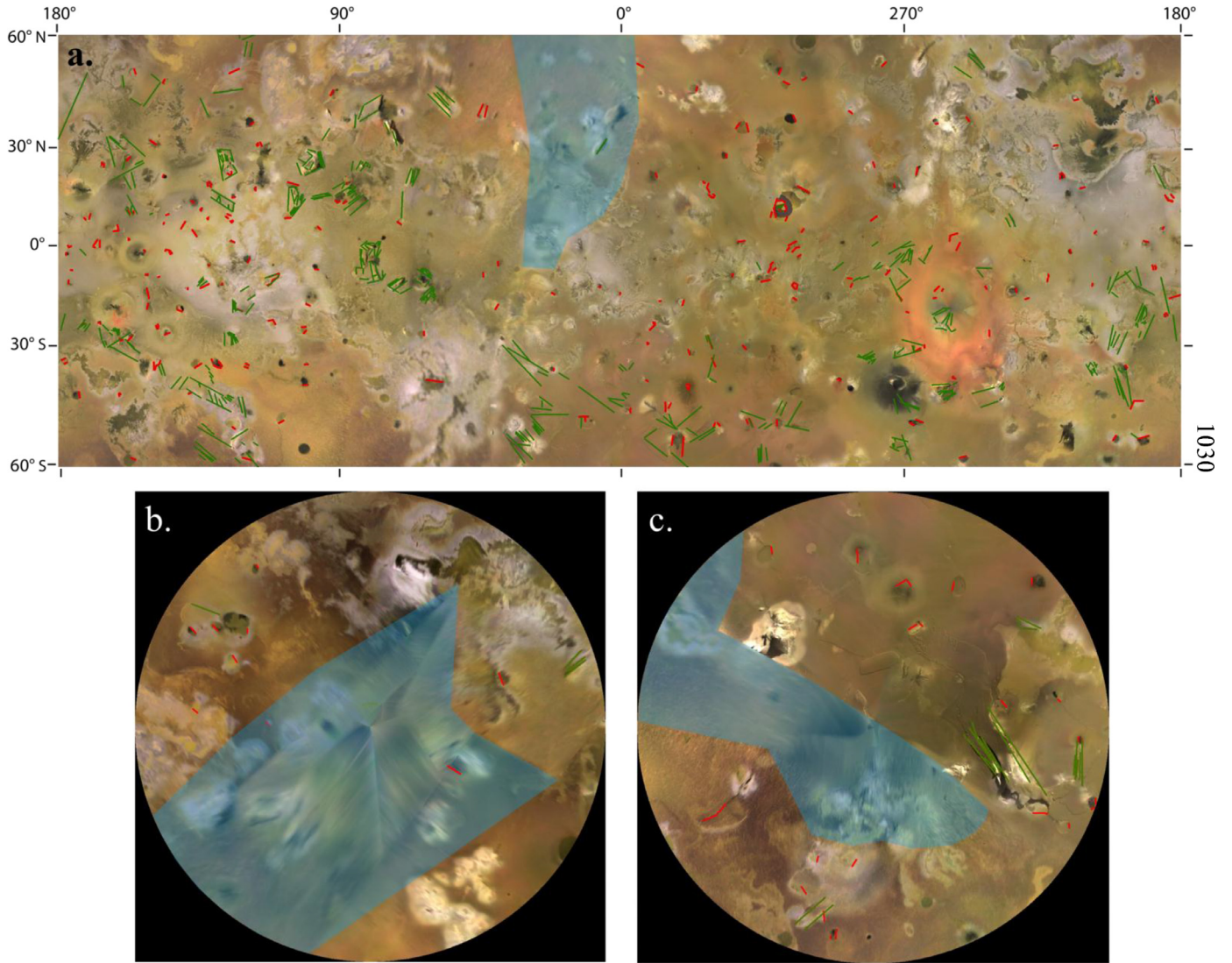


Fig. 2. Global lineations. (a) Structural lineations (green) and patera-edge (red) lineations on Io. (b) Lineations in the north pole mosaic. (c) Lineations in the south pole mosaic. Blue shaded regions indicate areas of lower resolution (> 21 km/pixel). (For interpretation of the references to colour in this figure legend, the reader is referred to the web version of this article.)

where n is the total number of pairs of azimuths and lengths and r_i is the corresponding circular rank (smallest to largest) of the azimuth measurements following the approach of Tu (2015) and others (Johnson and Wehrly, 1977; Tasdan and Cetin, 2013). We then calculated T_c and T_s , which are terms used in calculating both correlation coefficients and scaled correlation coefficients as defined by Batschelet et al. (1973):

$$T_c = \sum_{i=1}^n x_i \cos(\beta_i)$$

$$T_s = \sum_{i=1}^n x_i \sin(\beta_i)$$

where x_i is the rank of the length measurements. Finally, we calculated the correlation coefficient, R , given by:

$$R = \frac{24(T_c^2 + T_s^2)}{n^2(n+1)} \approx \chi^2 \text{ as } n \rightarrow \infty$$

using the values we obtained for T_c and T_s above. To scale to traditional R-values between -1 and 1 , transformations were

performed for when n is even and odd, respectively, given by:

$$a_n = \frac{1}{1 + 5\cot^2\left(\frac{\pi}{n}\right) + 4\cot^2\left(\frac{\pi}{n}\right)}$$

and

$$a_n = \frac{2\sin^4\left(\frac{\pi}{n}\right)}{\left(1 + \cos\left(\frac{\pi}{n}\right)\right)^3}$$

We used values obtained for a_n to calculate a scaled correlation coefficient, given by:

$$D_n = a_n(T_c^2 + T_s^2).$$

Lastly, the relationship between straight patera margins and mountain locations was tested to determine possible genetic connections. We used three different tests—the Equality Function, an independence test, and a random labeling test. The Equality Function measures how similar events are at different distances. Values greater than 1 indicate that features that are closer together tend to be of a similar type—that is, the closest features all tend to be mountains or all patera edges (Gelfand et al., 2010; Diggle, 2013). The independence test looks at whether the locations of

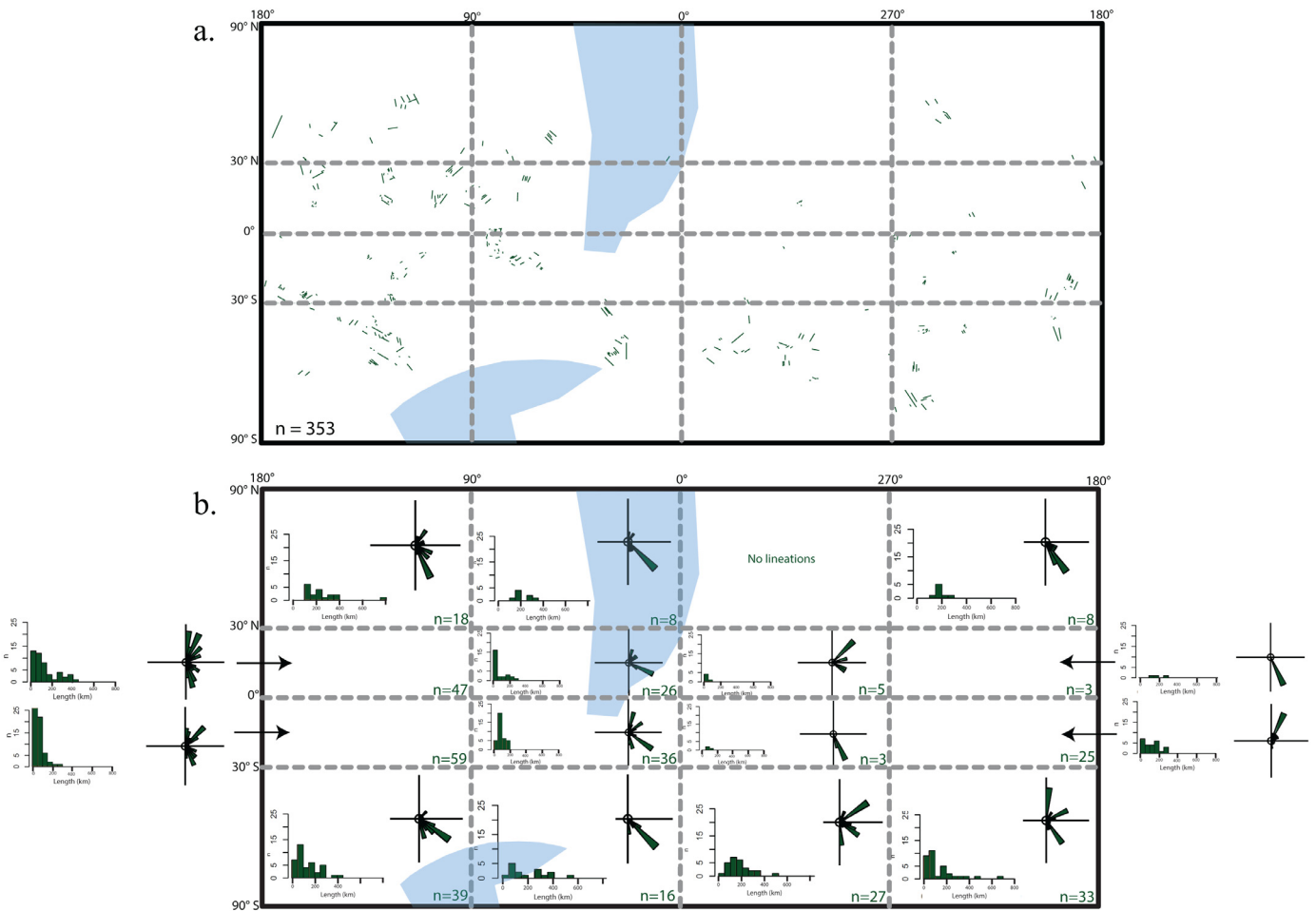


Fig. 3. (a) Approximate orientations of all structural lineations on Io identified in this study. Blue shaded regions indicate areas of lower resolution. (b) Structural lineation lengths and azimuths in each equal area sector. Longitude is measured in °W. (For interpretation of the references to colour in this figure legend, the reader is referred to the web version of this article.)

the individual points are independent of one another statistically, assuming a null hypothesis that the locations of the features are spatially independent of each other (Gelfand et al., 2010; Diggle, 2013). Finally, a random labeling test compares the locations of features of the same type with random reassigned locations (Gelfand et al., 2010; Diggle, 2013). Predicted bounds were again generated for our tests using 100 randomized scenarios.

The spatial statistics and feature identifications conducted in this study build on geologic mapping and measurements made on the Io ArcGIS Project by Williams et al. (2012), a lineation study by Radebaugh et al. (2011), mountain spatial measurements by Schenk et al. (2001), a comprehensive patera study by Radebaugh et al. (2001), and spatial analyses of mountains and volcanic features conducted by Kirchoff and McKinnon (2009), Kirchoff et al. (2011), and Hamilton et al. (2013). Additionally, we updated and reclassified some features on a database of paterae and mountains created by Barth and Radebaugh (2010). Areas of low resolution may affect the confidence level of some of statistical results; those are identified. Nevertheless, Io has sufficient image coverage such that our results are still statistically significant when comparing features identified on images of varying resolution. If there were higher resolution images of low-resolution areas, it is expected that the results would remain largely the same, but that uncertainty would decrease.

3.3. Results

3.3.1. Structural lineations

We identified 353 structural (non-patera) lineations on Io. Their lengths (total: μ (mean) = 129 km \pm 110 km) and azimuths (total: μ = 164° \pm 132°) are shown in 16 sectors of equal area in Fig. 3. Most structural lineations occur between 60° S and 30° N, and those between 15° S and 0° are shorter than at other latitudes (μ = 93 km \pm 45 km; Fig. 3b). There does not seem to be a statistically significant latitudinal pattern of azimuths of structural lineations (Fig. 3b). The highest frequency of structural lineations longitudinally occurs between 180°W and 240°W. Lengths and azimuths do not appear to show longitudinal patterns, except for a cluster of lineations with azimuths oriented at roughly 130° (SE) between 300°W and 330°W.

The patterns visible in Fig. 3a reveal that structural lineations exhibit clustering by location, and we have confirmed this statistically through the G and K functions (Fig. 4). In both cases, the observed values of the G and K functions far exceed the predicted bounds of complete spatial randomness (CSR), as shown by the gray bands. This indicates strong clustering of identified linear structures.

We used conditional marked moments for lengths of structural lineations to estimate the geographical extent of lineation trends (Fig. 4c). Lineations having a neighbor within 500 km tend to be shorter (μ = 100 km) than the global average (μ = 129 km

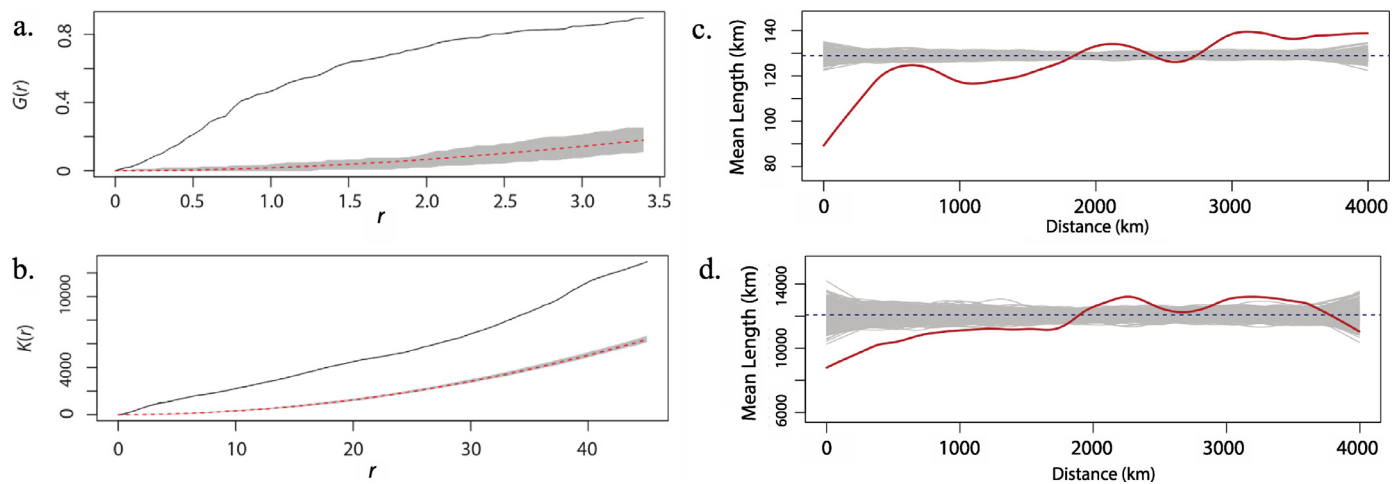


Fig. 4. Comparison of G (a) and K (b) functions for structural lineation nearest neighbors. r is the radius of the circle outlining cutoff distance in km. The predicted bounds for random spacing for both functions are represented by gray shading, with the average predicted values for each function represented in the middle of those bounds by the red dashed line. Observed values for structural lineations measured and calculated in this study are shown by the dark gray line. Both functions indicate strong clustering of structural lineations. (c) Conditional marked moments of structural lineations show the conditional mean, with global average and bounds indicated by the dashed blue line and the gray band, respectively. The red line indicates the values measured and calculated for the structural lineations in this study. (d) The conditional variance, with global average and its bounds indicated by the dashed blue line and the gray band, respectively. The red line indicates the values measured and calculated for the structural lineations in this study. (For interpretation of the references to colour in this figure legend, the reader is referred to the web version of this article.)

± 110 km). Those having a neighbor within 2000 km are still shorter than the average, but not as short as those with a very close neighbor. Lineations with a neighbor more than 3000 km away tend to be longer than the global average. The maximum distance between any features on Io is half of the moon's circumference, or 5722 km. Conclusions drawn about lineations at distances of 3000 km to 5722 km apart may not be as useful statistically, given that the low resolution areas will be encountered at some point measuring away from all lineations. Nevertheless, the close neighbor results remain valid. The variations between lineation lengths have a similar pattern (Fig. 4d). Lineations with closer neighbors tend to have a smaller variance, and are therefore more similar in length, than lineations with neighbors farther away.

Azimuth values between $75\text{--}100^\circ$ (E) and $165\text{--}180^\circ$ (S) for structural lineations are significantly less common (Fig. 5). The consistency of these orientations and their roughly perpendicular relationship suggest that a global stress field may play a role in the formation of many structural features on Io. The 90° offset between dominant orientations may suggest one overall stress regime (with petal concentrations perpendicular to the directions of σ_1 and σ_2) or two different stress regimes occurring at different times from one another (with petals both indicating the direction of σ_1 for each stress regime). Variation in the azimuths of the structures may also be controlled by local subsurface structures, crustal anisotropies, or volcanic activity.

Lengths and azimuths of the structural lineations do not appear to be related. We obtained a p-value for our null hypothesis of no relationship of 0.764, suggesting the null hypothesis is valid and there is no relationship between the lengths and azimuths of structural lineations. Thus, it is unlikely that a single major stress orientation is responsible for creating the largest structural features globally on Io. Instead, orientations and lengths of tectonic features as a whole may be controlled both by large-scale stress regimes and by local subsurface structure or crustal anisotropies.

3.3.2. Patera-Edge lineations

We measured 306 patera-edge lineations and analyzed them in the same way that we did structural lineations. 193 paterae, or 41% of the total paterae identified, have at least one straight margin, and paterae with straight margins occur most frequently at lower latitudes. Higher numbers of paterae are also found at

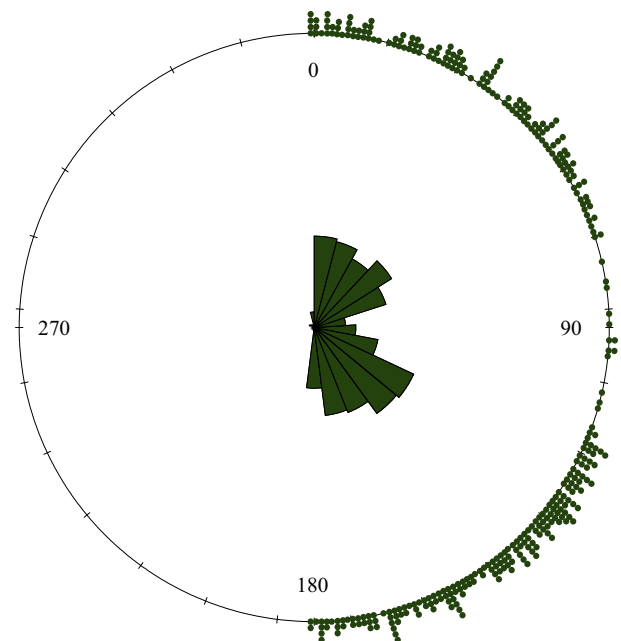


Fig. 5. Orientations of all observed structural lineations on Io. The lengths of the bars are determined by numbers of lineations within the bins. Internal bar bins are every 15° , external bins are every degree.

low latitudes (Radebaugh et al., 2001), however, which was not corrected for in this study. Longitudinally, straight patera margins occur most commonly between 180° W and 90° W and between 300° W and 0°

Globally, paterae with straight edges cluster (Fig. 6) as revealed by comparison with the G and K functions (Fig. 7a, b). Patera-edge lineations have shorter average lengths ($\mu = 43$ km, $\sigma = 27$ km) than structural lineations overall; nevertheless, like the structural lineations, they are slightly shorter ($\mu = 38$ km, $\sigma = 23$ km) than the average at lower latitudes (Fig. 6). Additionally, patera edge lengths are also shorter than the global average where they have a neighboring patera with a straight edge within 2000 km. For example, the mean length for a random patera edge lineation with

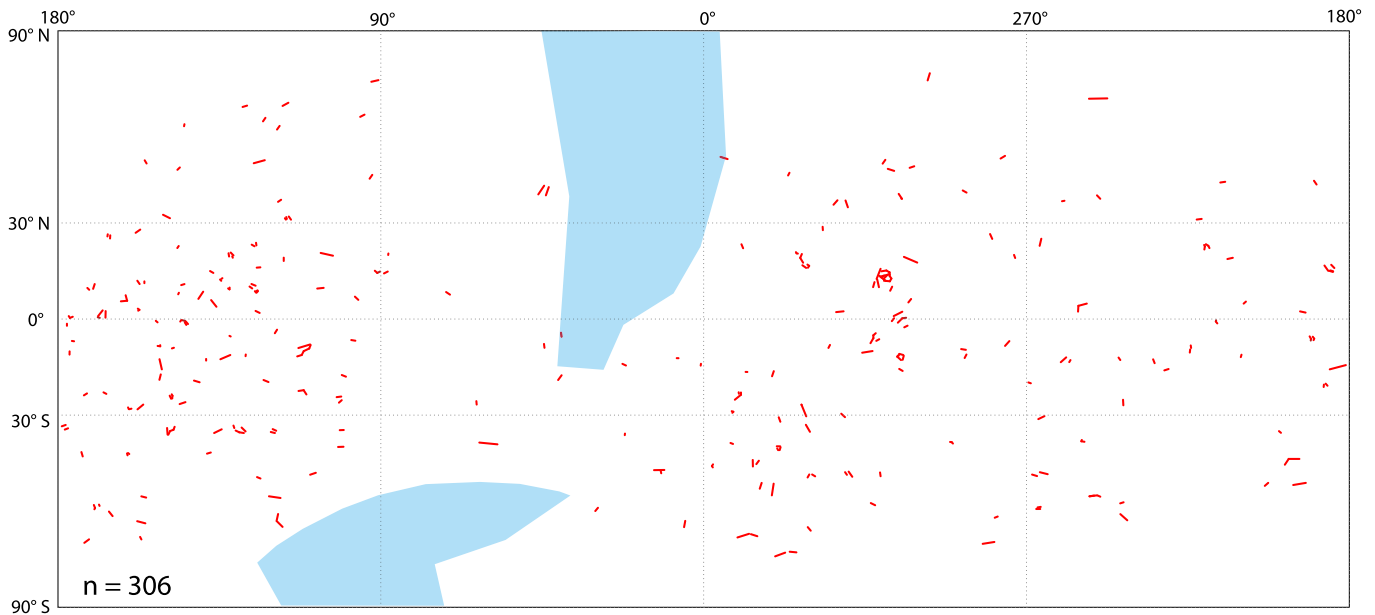


Fig. 6. Approximate orientations and lengths of patera-edge lineations on Io. Blue shaded regions indicate areas of lower resolution (> 21 km/pixel).

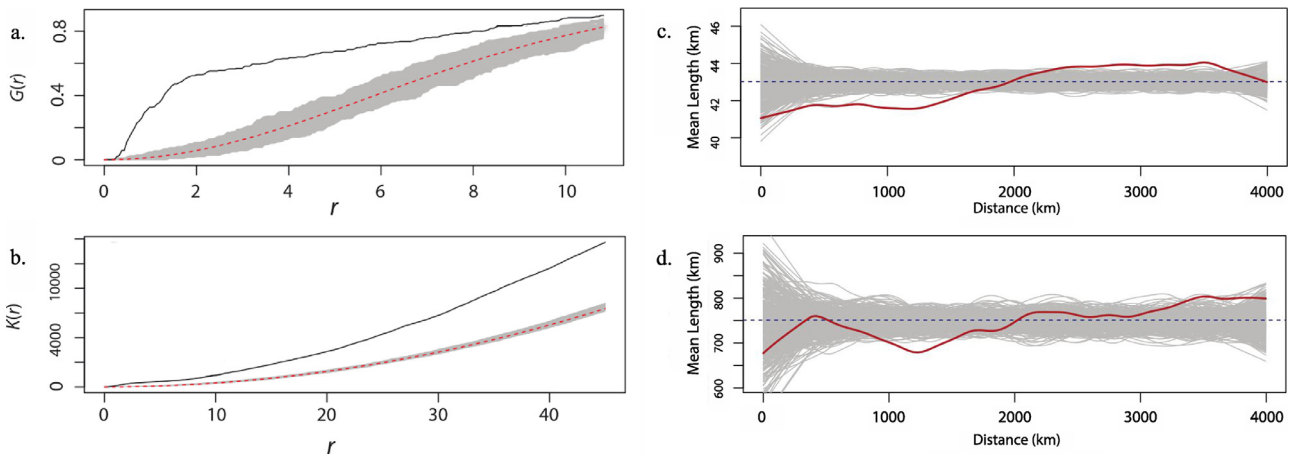


Fig. 7. Comparison of G (a) and K (b) functions for patera-edge lineation nearest neighbors. The predicted bounds of both functions are represented by gray shading, with the average predicted values for each function represented in the middle of those bounds by the red dashed line. Observed values for straight patera edges are shown by the black line. Both functions indicate strong clustering of patera-edge lineations. Again, in (a) and (b), r represents a given cutoff distance between features. (c) shows the conditional mean of edge lengths, with global average and its bounds indicated by the dashed blue line and the gray band, respectively. The red line represents the measured lengths as a function of separation distance for the patera-edge lineations. (d) shows the conditional variance of length, with global average and its bounds indicated by the dashed blue line and the gray band, respectively. The red line indicates the lengths of the patera edge lineations measured in this study. (For interpretation of the references to colour in this figure legend, the reader is referred to the web version of this article.)

a neighbor 100 km away is ~ 40 km, and for a lineation with a neighbor 1000 km away is ~ 42 km, just slightly smaller than the global average. The variance, however, is not statistically different from what we would expect if there were no relationship between the locations of lineations and length (Fig. 7d).

In contrast to structural lineations, patera edge lineation azimuths have no significant, global preferred orientations (Fig. 8). This indicates that collapse within paterae along straight margins may not be caused by a global tectonic regime, but rather is governed by localized stresses or the orientations of local subsurface structures.

There also seems to be little relationship between the global location of a patera edge lineation and its azimuth. However, using the same nonparametric circular-linear correlation between length and azimuth, we obtained a p -value of 0.052. We therefore cannot reject the null hypothesis of no relationship between the lengths and orientations of straight patera edges; with the small

but inconclusive p -value, further investigation into the possibility of a relationship may be necessary.

Generally, paterae with straight margins have higher aspect ratios (length: width) because straight margins prevent paterae from being very circular. However, although patera edge lineations may be considered indicators of tectonic features, such as faults or fractures, we do not consider paterae themselves to be useful strain indicators. We do not have sufficient context for paterae and any nearby tectonic features, so it would be inappropriate to assign tectonic processes or crustal stresses to an area based off of long and short patera axes.

3.3.3. Mountain spatial statistics

Mountain widths and areas are smaller at low (15°S to 15°N) latitudes (width: $\mu = 89 \text{ km} \pm 39 \text{ km}$; area: $\mu = 13,100 \text{ km}^2 \pm 10,895 \text{ km}^2$) and poleward of 60°S (width: $\mu = 67 \text{ km} \pm 39 \text{ km}$; area: $\mu = 7557 \text{ km}^2 \pm 6200 \text{ km}^2$) than average ($109 \text{ km} \pm 60 \text{ km}$;

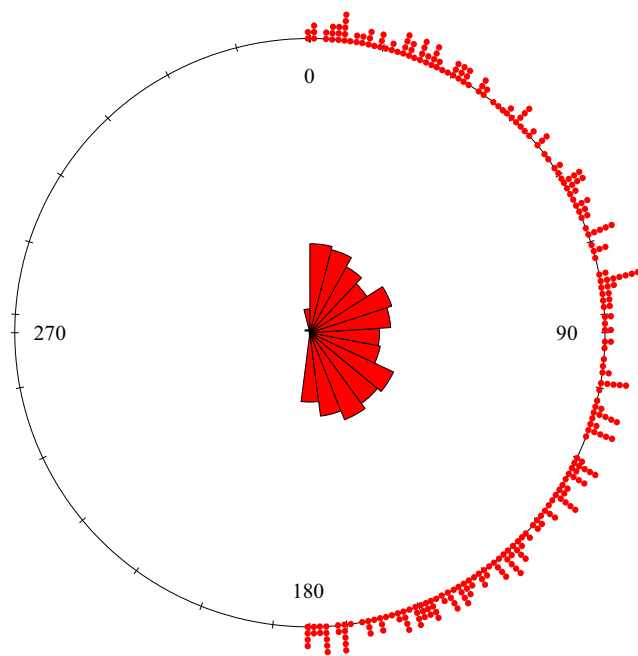


Fig. 8. Orientations of patera edge lineations. The lengths of the bars are determined by numbers of lineations within the bins. Internal bar bins are every 15° , external bins are every degree.

and $20,810 \text{ km}^2 \pm 21,500 \text{ km}^2$; respectively). There seem to be no statistical patterns in mountain lengths, widths, or areas by longitude. Moreover, no statistically meaningful patterns are apparent in relating the distances between mountains and their lengths, widths, or areas. In summary, mountains are relatively isolated, varied in size and shape and have no significant geographic patterns in those variations save for broad concentrations of mountains around 90° and 270° (Schenk et al., 2001; Kirchoff et al., 2011). Long axes of mountains, which should be related to orientations of maximum and minimum stress, do not possess any distinguishable global patterns; rather, axes of similar orientations cluster locally. This may mean that even if a global stress regime causes or influences orientation of mountain formation, the response to global stresses varies according to local subsurface features. These statistics are limited by low image resolution for some areas, which have prevented us from decisively constraining the dimensions of the remaining ~ 53 mountains identified by Schenk et al. (2001) and Jaeger et al. (2003).

3.3.4. Patera spatial statistics

Our updated patera catalog supports the findings of Radebaugh et al. (2001), Kirchoff et al. (2011), and Hamilton et al. (2013) that the majority of paterae are found at low latitudes (with 57% of paterae between 30°S and 30°N , which contains half the surface area of Io). Although they occur more frequently, paterae in this latitudinal band are smaller ($\mu = 2932 \text{ km}^2 \pm 4015 \text{ km}^2$) than the global average ($4595 \text{ km}^2 \pm 6902 \text{ km}^2$).

There does not seem to be a longitudinal pattern of patera sizes (perimeters or areas); however, between 260°W and 0° more paterae occur that have 50% or 100% floor coverage by dark lava (thought to be young; Fig. 9). This marks regions with more active volcanism possibly associated with tidal dissipation (Ross et al., 1990; Segatz et al., 1988; Tackley et al., 2001) or with subsurface structures allowing magma to migrate to the surface more easily. In their patera database, Barth and Radebaugh (2010) classified paterae based upon amount of floor coverage—in bins of 0, 50, and 100% floor coverage by lava. We mapped and tested these for spatial patterns. Paterae with significant floor coverage ($\geq 50\%$) do

not seem to have the same distribution as hotspots across Io, yet this remains mostly unexplored. Further comparison of hotspot distribution and patera floor coverage may lead to increased understanding of the nature of volcanism both globally and locally, and constrain the location and movement of magma below the surface.

Patera separation distances were also evaluated with the G function, and they plot within the region predicted for random spacing. It is possible that paterae cluster on different scales. Paterae with a close neighbor have smaller perimeters than the global average ($\mu = 227 \text{ km}$, $\sigma = 154 \text{ km}$), but larger variances than we would expect. For example, paterae with a neighbor 1000 km away have a mean perimeter of about 200 km and a standard deviation of about 140 km. Paterae with a neighbor 100 km away have a mean perimeter of about 215 km but a standard deviation of 173 km.

We used pairwise Wilcoxon tests (Lowry, 2015) to detect patterns between patera size and amount of floor coverage. Paterae that exhibit 100% floor coverage are smaller in size ($\mu = 2847 \text{ km}^2$, $\sigma = 4604 \text{ km}^2$), while paterae with floors that are either 50% ($\mu = 4604 \text{ km}^2$, $\sigma = 6393 \text{ km}^2$) or 0% covered ($\mu = 5521 \text{ km}^2$, $\sigma = 8566 \text{ km}^2$) have larger areas. Whether this is a result of smaller paterae being easier to fill with lava or an indication that regions with smaller paterae are more active is not clear at this point but merit further investigation.

3.3.5. Patera edge lineations and mountains

We tested the relationships between the locations of straight patera margins and mountains to identify the influence of different stress fields in mountain formation and patera collapse, and to determine if a genetic relationship exists between mountains and paterae with straight, and possibly tectonically created, margins. This was done with three different tests—the Equality Function, an independence test, and a random labeling test. Fig. 10a shows the results of the Equality Function analysis. A value of 1 suggests there is no relationship between the location and type of feature. The values of the Equality Function for our data are greater than 1, so statistically, features closer to each other tend to be of similar types. In other words, mountains are generally closer to each other than to straight patera margins. The same is true for straight patera edges, but this result is biased by the fact that many paterae have more than one straight edge to their margins, which were each measured as separate lineations. Therefore, the number of straight patera margins in one location may not reflect the number of paterae with straight margins occurring there, but rather the total number of straight patera edges in that location. The independence test looked at whether statistical processes determining the locations of mountains and straight patera edges were similar (Fig. 10b). All mountain locations and all patera edge locations were paired with each other and inserted into their respective parameters in the independence function. Because these plot within the bounds predicted for random relations, we can conclude that the null hypothesis of independence in what determines the locations of mountains and straight patera margins is valid. That is, mountains and patera edges have been shown to form statistically independent of one another. The random labeling test yielded a similar result to that from the Equality Function (Fig. 10c), indicating no statistical relationships between the locations of paterae and mountains.

It appears that locations of mountains and patera edge lineations are significantly different than they would be from random assignments individually and that features close to each other tend to be of the same type. Therefore, paterae with straight edges are often closer to other paterae with straight edges, rather than to mountains. This may be due to the nature of having many more paterae than mountains on Io's surface. It seems that mountains and paterae may be genetically related in some cases, but we

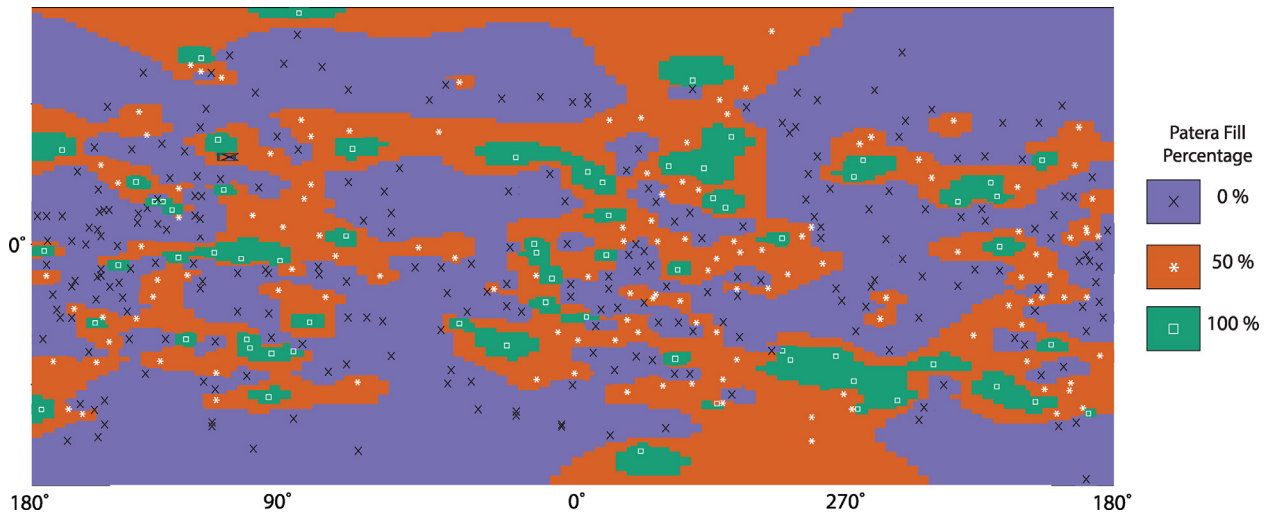


Fig. 9. Global map showing the percent fill of patera floors, smoothed according to location. The symbols x, *, and □ represent the locations of paterae with 0, 50, and 100% floor coverage, respectively. The x-axis is measured in degrees west longitude and the y-axis extends to 90°N and S latitude. (For interpretation of the references to colour in this figure legend, the reader is referred to the web version of this article.)

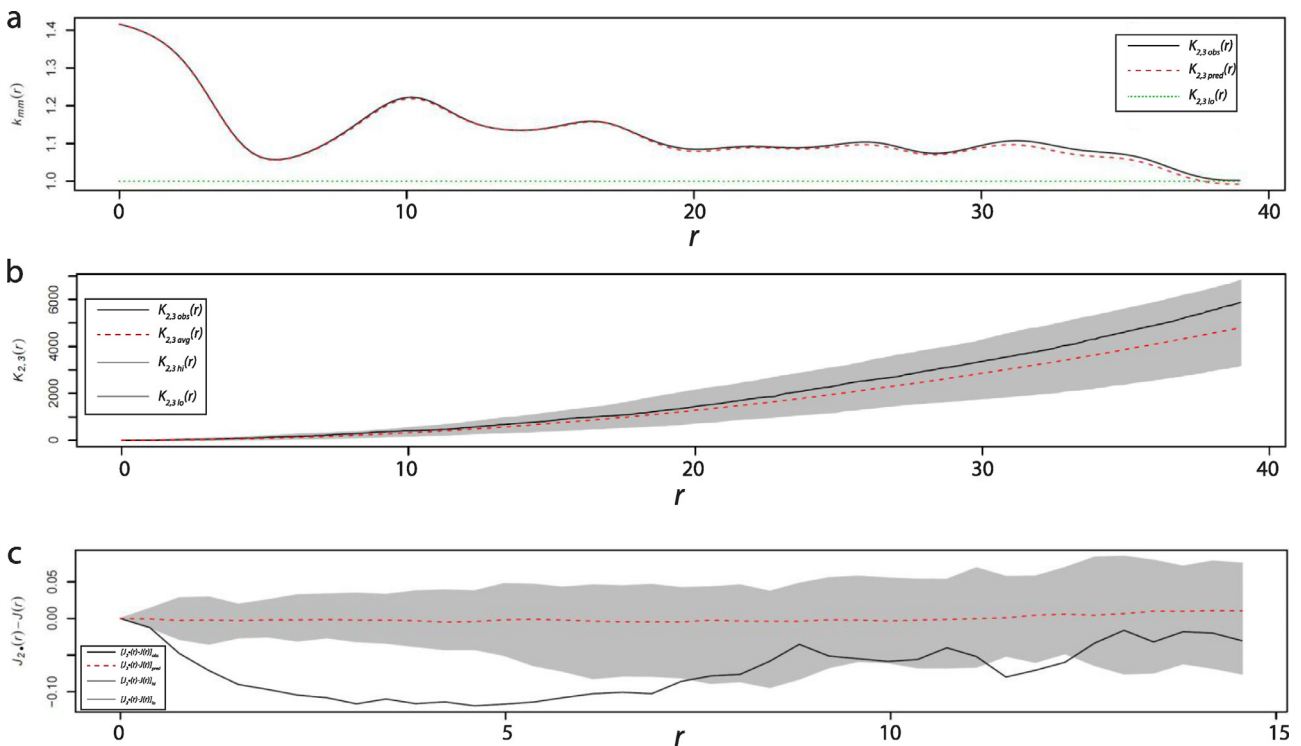


Fig. 10. Relationships between mountains and patera edge lineations as revealed by (a) equality function, (b) independence test, and (c) random labeling test. Predicted average values are shown as the red dashed line and predicted bounds for random associations are represented by gray bands. Black lines indicate results from this study. r is the normalized radius of a circle away from each data point. (For interpretation of the references to colour in this figure legend, the reader is referred to the web version of this article.)

cannot conclude that mountains and paterae that appear structurally controlled are always found in close association. There may be processes independent of mountain formation and evolution causing paterae to collapse along straight, sharp margins.

4. Structural mapping

To better understand mountain-patera interaction, we constructed structural maps of smaller regions to determine processes driving the formation of these two features.

4.1. Methods

High-resolution (200–300 m/pixel) images from Galileo SSI were used to identify and interpret structures and to construct structural maps for 4 regions: Hi’iaka Montes, Shamshu Mons, Tohil Mons, and Zal Montes. These locations were selected based on the resolution of the images, the tectonic complexity, and the potential for insight into crustal deformation patterns and stress input. This work uses similar conventions to, and builds upon, geomorphic mapping by Bunte et al. (2008), Bunte et al. (2010), and Williams et al. (2002; 2004). The base images of the maps have been projected orthographically to eliminate distortions us-

ing both ArcGIS and the USGS Map Projection on the Web (POW) (Hare et al., 2013). We then identified important tectonic or topographic features in these images and classified them as reverse faults, normal faults, grabens, strike-slip faults, mass wasting or landslide scarps, and erosional scarps. Our interpretations of the types of structural features were based on shadow observations, sense of displacement of features, scarp shape and morphology, and terrestrial tectonic analogs. Cross sections were generated for three of the four areas with as little vertical exaggeration as possible while preserving sufficient topographic detail. The cross sections consider the lithospheric thickness, or rather, the thickness of the uppermost brittle layer of Io, to be about 30 km based on previous studies (Keszthelyi and McEwen, 1997; Jaeger et al., 2003; Leone et al., 2011; Jozwiak, 2014).

4.2. Results

4.2.1. Structure of Hi'iaka Montes

The Hi' iaka Montes are located at 3.5°S, 79.5°W with two large mountains located atop what appears to be a larger crustal block (Fig. 11). The block (~135 km x 340 km; width and length of inferred crustal block) contains North Hi' iaka (11 km high; Schenk et al., 2001) and South Hi' iaka (4.3 km high; Schenk et al., 2001; Turtle et al., 2001) Montes, the two L-shaped mountains in the center of the image, and West Hi' iaka Mons, the small peak isolated in the basin just west of South Hi' iaka Mons (Fig. 11a). Hi' iaka Patera (60 km x 95 km; short and long axes, respectively) resides in the basin just east of North Hi' iaka Mons and Mekala Patera (55 km x 20 km) next to its southwest corner (Bunte et al., 2010). North Hi' iaka Mons is distinguished by parallel ridges running N-S along the top of the plateau and additional tall ridges running NW-SE on its northern margin (Fig. 11a). Younger volcanic layers cover many of the important structures or crustal block boundaries in the surrounding region (Fig. 11b), a result of Io's constant and rapid resurfacing (Johnson et al., 1979; McEwen et al., 1989). Therefore, it is not entirely clear how the Hi' iaka crustal blocks are interacting with other regions of the crust around them or the precise locations of some faults. Therefore, we draw conclusions from those structures and related features that are currently visible.

We propose that high-angle reverse faults bound the western and eastern sides of this crustal block (Fig. 11). These are morphologically similar to blocks bounded by high-angle reverse faults that cut the deep basement of Wyoming's Laramide folds and mountain ranges (Dickinson and Snyder, 1978) in that the blocks are largely deformed on their edges and possess both compressive uplifts and basins with steep, straight reverse faults. The sub-parallel features on the top of the Hi' iaka plateaus are tens of meters deep and tens of meters across (Bunte et al., 2010). It is possible that these features are small-wavelength folds with orientations reflecting the orientation of σ_1 , although the rigid properties of the upper crust may prohibit formation of such small-scale folds. Moore et al. (2001) suggested that these features were created due to downslope motion of weak layers probably made of plume deposits (2001). However, we propose that these features are grabens formed from extension above the neutral surface of the fold and have been labelled as such in Fig. 11. This interpretation is based on terrestrial observations of broad uplifts associated with high-angle reverse faults, such as those in the Owl Creek uplift of central Wyoming (see Fig. 15). Crustal shortening may have resulted in uplift of the Hi' iaka Montes and extension across the top surfaces, with the formation of keystone grabens on North Hi' iaka Mons (Wise, 1973).

After the initial episode of horizontal shortening, additional shortening of the crust in this area oblique to the bounding reverse faults has produced a dextral strike-slip fault running between the

two mountains, breaking apart the larger crustal block (Fig. 11). This is based on interpretations made by Jaeger et al. (2003) and Bunte et al. (2010) and by further identification of features associated with a strike-slip system in this study. We propose that the northern arm of North Hi' iaka Mons has accommodated oblique strike-slip motion on restraining bends (Fig. 11a) by construction of the NW-trending ridges that make up the highest elevations in the area, up to 11 km (Schenk et al., 2001). The transpressional features in this area are similar to the transpressional ridges running through Damascus and Palmyra, Syria formed along a restraining bend in the strike-slip Dead Sea Fault (Mann, 2007). The way transpression is accommodated mostly by vertical displacement is also analogous to structures adjacent to the San Andreas Fault zone (another strike-slip fault) near San Bernardino, California (Spotila et al., 1998). Deformation on the north side of North Hi' iaka Mons also looks as though it may have bent the localized extensional features on the top of the plateau (Fig. 11a). If this interpretation is correct, it suggests that the grabens formed either just before or simultaneously with strike-slip movement.

On the southern edge of South Hi' iaka Mons, a very different response to fault movement seems to have occurred. Instead of transpressional features building up tall peaks, normal faults and extensional collapse have shaped the southern edge. A large valley separates the northern, apparently more cohesive part of the mountain from the more friable, collapsing side on its southern end. Extensional faults and gravitational failures parallel to the southern arm of South Hi' iaka Mons indicate the main processes in this area are rifting and collapse (Fig. 11a). The apparent difference between the northern edge of North Hi' iaka Mons and the southern side of South Hi' iaka Mons may be due to crustal anisotropy or differential rate of movement along the faults in the area. Perhaps South Hi' iaka Mons has not met the same type of resistance in the crust as the north mountain, a result of either composition or structures buried by voluminous volcanic layers.

In addition to producing transpressional features, we conclude that the dominant stress regime also opened transtensional basins on the eastern side of North Hi' iaka Mons and the western side of South Hi' iaka Mons. An active patera (Hi' iaka Patera) formed in the northeastern basin, possibly facilitated by the rifting and thinning of the crust that occurred as a result of strike-slip movement on the bounding faults (Fig. 11).

In the northeastern basin, late and minor shortening apparently occurred, as indicated by long arcuate scarps that we relate to reverse faults adjacent to the eastern side of North Hi' iaka Mons (Fig. 11a). These thrusts must have formed after or during strike-slip motion because they are overprinted on the basin-filling deposits.

West Hi' iaka Mons, a small peak in the southwestern basin, may have separated from southern Hi' iaka Mons in a similar fashion to the break off and isolation of Madagascar from the northward-moving Indian plate. An alternate origin is that of an erosional remnant, and at this point the origin of West Hi' iaka Mons remains unclear.

It is unclear whether there is a significant relationship between South Hi' iaka Mons and Shamshu Mons, which lies ~70 km southeast of the southeastern corner of South Hi' iaka Mons. The southern arm of South Hi' iaka Mons is parallel to the long axis of Shamshu, but the features on each mountain do not seem to indicate that they are in tectonic "communication." The plain between the two may contain a buried major reverse fault separating the Hi' iaka block and the Shamshu block and keeping the two mountains from interacting directly with one another. If so, it is unlikely that the Hi' iaka Montes complex is directly causing the uplift of Shamshu Mons.

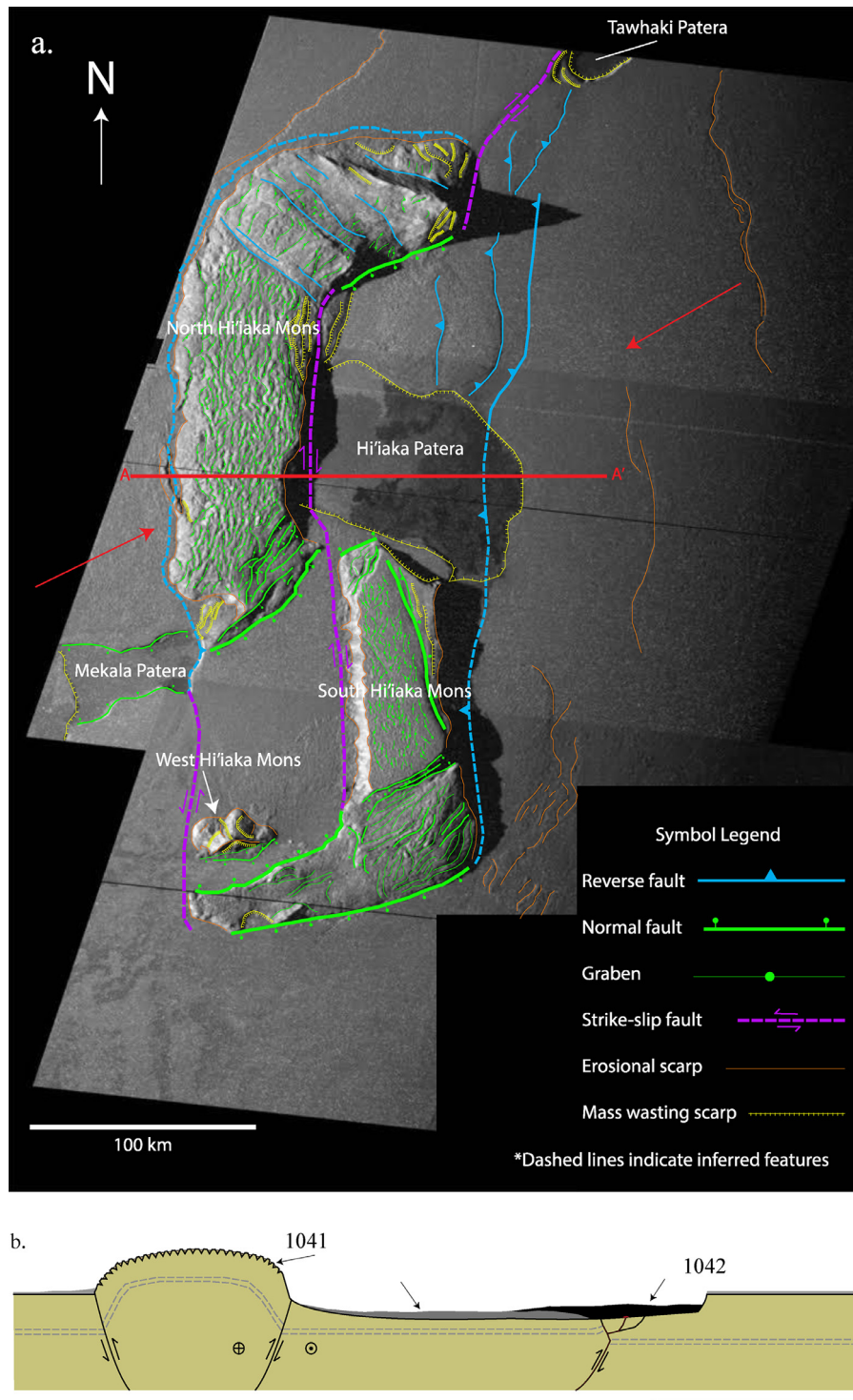


Fig. 11. Hi'iaka Montes region of Io (3.5°S, 79.5°W). (a) Reprojected Galileo image (~250 m/pixel) of the Hi'iaka Montes complex with structural interpretations (previous page). Image was obtained during the I25 flyby on November 26, 1999. Illumination from the left (west). The red arrows indicate proposed orientations of principal horizontal stresses, σ_1 . (b) Cross section (above) from A to A' (a) across North Hi'iaka Mons and Hi'iaka Patera. Fresher eruptions on the patera floor are black and older flows are gray. The dashed gray line represents the behavior of crustal layers in the subsurface. Mountain bounding faults are interpreted to have oblique slip with strike-slip and reverse movement as a result of global contraction due to subsidence. The vertical axis is unscathed but vertical exaggeration is about 2x. (For interpretation of the references to colour in this figure legend, the reader is referred to the web version of this article.)

In summary, the tectonic history of the Hi'iaka region appears to be governed by largely buried, pre-existing faults in the deeper crust that were reactivated obliquely by continued shortening of the crust. It seems most likely that North and South Hi'iaka Mons are part of a large, coherent crustal block that has been uplifted and modified, with maximum stresses at oblique angles

to faults previously formed and then buried by volcanic deposits. Loading by volcanic deposits on a global scale and subsequent horizontal shortening of the crust was a hypothesis presented by [Schenk and Bulmer \(1998\)](#) in their discussion of the Euboea Montes area. The idea of strike-slip modification in the Hi'iaka area was discussed by [Bunte et al. \(2010\)](#) in their geomorphic

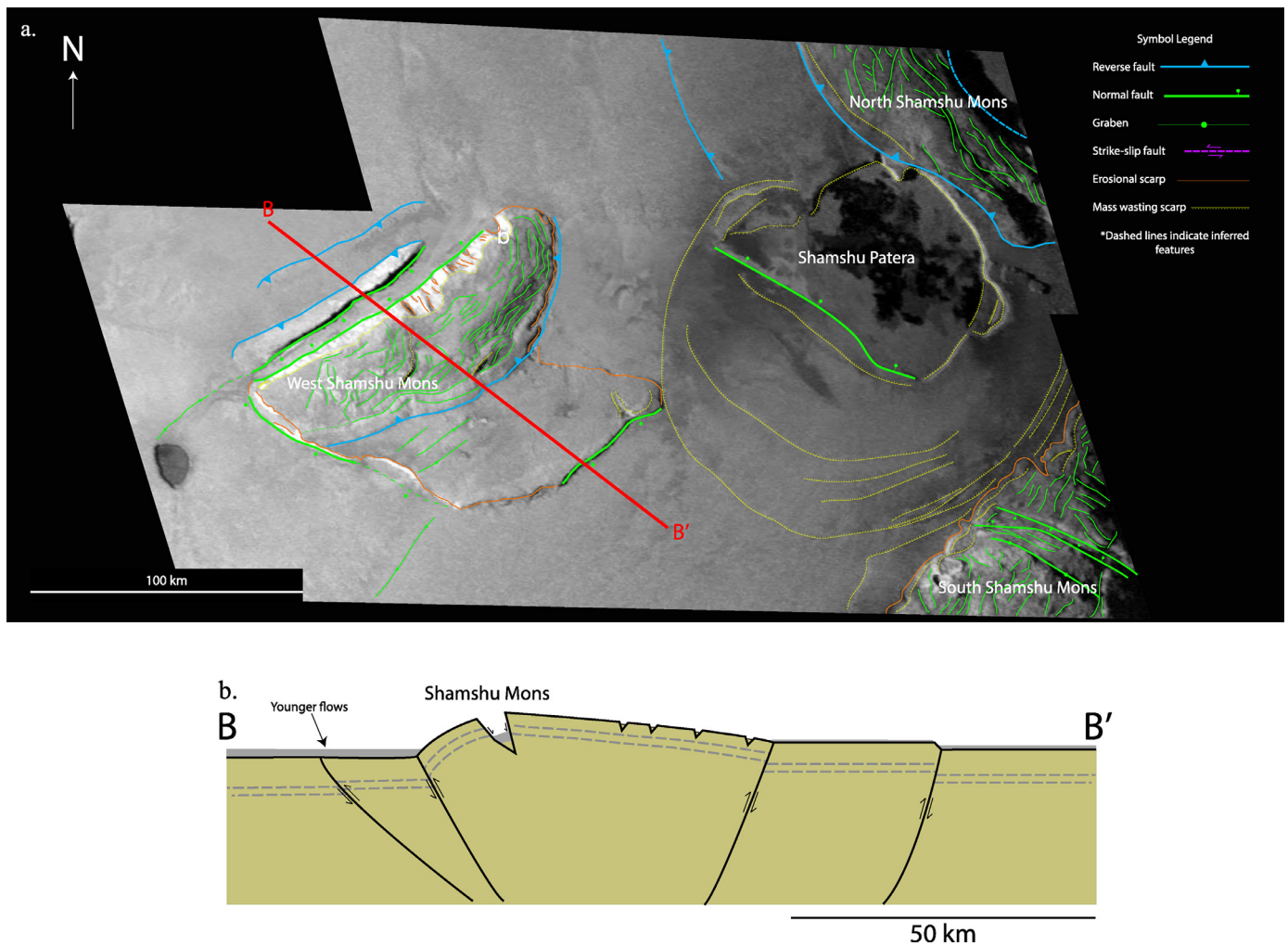


Fig. 12. Shamshu Mons and Patera (9.0°S, 68.0°W). (a) Reprojected mosaic of Galileo images (~345 m/pixel) of the Shamshu region and structural interpretations (previous page). Image was obtained during the I27 flyby on February 22, 2000. The red arrows indicate proposed orientations of principal horizontal stresses, σ_1 (left). (b) Cross section from B to B' (right) as indicated on (a). The dashed gray line represents the behavior of crustal layers in the subsurface. The vertical axis is unscaled but vertical exaggeration is about 2x. (For interpretation of the references to colour in this figure legend, the reader is referred to the web version of this article.)

mapping. We build upon both of these concepts by combining them—shortening of the crust with maximum stress oblique to pre-existing basement faults has produced strike-slip motion and its associated features in this area.

4.2.2. Structure of Shamshu Mons and Patera

Shamshu Mons (~3 km high) and Patera (76 km x 61 km; long and short axes, respectively) lie just southeast of the Hi' iaka region at 9.0°S, 68.0°W. Two other mountains, northeast and southeast of Shamshu Mons and both unnamed, are separated from Shamshu Mons by Shamshu Patera. A smaller patera (14 km x 11 km) sits just southwest of the large valley on the northwestern slope of Shamshu Mons (Fig. 12a).

We have interpreted the arcuate features on the northwest and southeast sides of Shamshu Mons as reverse faults, based on their curvilinear natures and the contractional morphology of Shamshu Mons (Fig. 12a). Shamshu Mons is steeper on the northwest side, probably due to the asymmetrical nature of the underlying fold and associated thrust faults, or from differential movement along its faults (Fig. 12b). The southeast flank is also marked by gravitational slumps whose headwalls approximately parallel the crest of the massif. The NE-trending valley that runs through Shamshu Mons parallel to its long axis is likely a graben formed from localized extension above the neutral surface at the axis of the

asymmetric fold. Additionally, the floor of the graben in Shamshu Mons is smooth and at the same elevation as the surrounding plains, suggesting that it may have been resurfaced recently; dark flow lobes extend from the rim of the small patera to the north and fill the graben (Fig. 12). A fault terminates a plateau southeast of Shamshu Mons and separates it from the smooth plains containing Shamshu Patera. Its arcuate shape suggests that it is a reverse fault, which occurred late because it cut lava flows on the plain and then was partially buried by more volcanism (Fig. 12a).

Shamshu Patera appears to be bounded by randomly oriented collapses. The collapses do not show conclusive evidence that they are tectonic in nature, given that they are not very straight, nor do they continue beyond the margins of the patera. The arcuate features lying adjacent to the mountain in the southeast corner of the image (Fig. 12a) may be remnants of the patera's edges at one point in its history. They could have become less defined by sapping or erosion, collapse and mass wasting, or by infill of the patera when it may have been more active and before activity shifted to the east. Plains materials between these margins and Shamshu Patera have a slightly different texture, smoother and more akin to layered lava flows, than the surrounding plains, which is consistent with the history of infill of the patera.

We interpret the faults bounding the mountain to the northeast as reverse faults. Shamshu Patera has incised the side of

the northeast mountain adjacent to it, suggesting it is younger than the mountain. The top surface of that mountain is lineated and likely fractured due to localized extension from folding and uplift. The mountain in the southeast corner of the image is also heavily lineated (Fig. 12a). It too could be bounded by thrust faults, or by a normal fault on the side facing Shamshu Mons, which faults have lost surface expression due to fracturing, mass wasting, or the previous boundaries of Shamshu Patera (Fig. 12a). Without full context, we cannot tell the orientations of the long axes of the other mountains and therefore cannot say whether they could have previously been combined with Shamshu Mons to make one large mountain as suggested by Bunte et al. (2010), or if they were formed independently in separate fault-bounded blocks under similar or multiple stress regimes. From what the images reveal, the long axis of the northeastern mountain is perpendicular to Shamshu Mons and therefore may not have been formed by the same stress regime. The extensional fault on the southeast plateau adjacent to Shamshu Mons and the smooth plains between Shamshu Mons and the southeastern mountain may indicate rifting and subsequent volcanism have occurred between them. Unfortunately, subsurface structures are covered by multiple layers of volcanic material, obscuring a more complete interpretation of the tectonic history of the Shamshu region.

4.2.3. Structure of Tohil Mons

Tohil Mons (28°S, 161°W) is 350 km long and 5.4 km high (Schenk et al., 2001). To the east of its large summit “crater” lies Radekast Patera, with its dark, lava-covered floor, and farther east, the much larger Tohil Patera. Wabasso Patera also sits just northwest of Tohil’s northwestern-extending plateau (Fig. 13a). Tohil Mons is one of the most geologically complex mountains of Io’s surface and the region surrounding it is a site of active volcanic, tectonic, and degradational processes (Williams et al., 2004).

Tohil Mons likely sits on its own fault-bounded crustal block, although the complete extent of the block is unclear, as the plains surrounding the mountain complex have been resurfaced by volcanism (Williams et al., 2004). The mountain seems to be bounded by reverse faults, with a strike-slip fault running down its long axis (Fig. 13a).

Like Hi’ iaka, Tohil Mons was probably built and modified by shortening and strike-slip motion in a large, crustal block. Maximum horizontal stress was likely oblique to pre-existing NW-SE-trending basement faults and block-bounding faults, which induced strike-slip movement on what was probably a near-vertical fault. Graben-like features on the elongated plateaus of Tohil may be like those on the plateaus of the Hi’ iaka Montes, formed by extension above a neutral surface in a large fold or through gravitational slip (Fig. 13). This may also be how the extensional faults and grabens formed on the northeast lobe of Tohil Mons. The margins of Tohil have been eroded, possibly through SO₂ sapping, far more than those at Hi’ iaka seem to have been. The major faults bounding the Tohil block have likely been buried or obscured by erosional scarps, landslide material, or volcanic cover.

We suggest that Radekast Patera formed in a transtensional basin, opened as a result of dextral motion along the NW-trending strike-slip fault, similar to the way in which Hi’ iaka Patera formed. The sense of downward motion along the oblique-slip fault seems to be both to the northwest and to the southeast of its summit “crater”. Instead of being attributed to a multiple fault system, this difference in motion could result from a difference in topographic level between the two halves, in which the northeast side is higher. The northeast portion appears to be experiencing greater gravitational degradation by landsliding than anywhere else along the fault, further supporting the idea that this part of the mountain is higher or steeper or more active than other locations (Fig. 13a).

The central “crater” of Tohil Mons is the result of a large slump, whose material has both collected in the floor and been consumed by the formation of Radekast Patera (Williams et al., 2004). Other landslides extend to the northeast, probably onto the floor of Tohil Patera. On the western side of the depression, large amounts of slumped material have created large lobes and a ridge-forming scarp extending from the scarp crater wall to the southwest. The west-trending ridge may be made of more resistant material or could simply be the scar from the large landslides (Fig. 13a). It is possible that the ridge is a resistant dike, as it is in line with Radekast Patera and the fissure eruptions actively occurring on the floor of Tohil Patera when the image was taken, but no other features indicate that Tohil Mons is volcanically built or fed. It also seems plausible that the summit “crater” is a result of mass wasting, since it is surrounded by slumped material.

A large-offset, steep, normal fault appears to have formed the northwest margin of Tohil, aligned with Wabasso Patera, possibly feeding magma to that area (Fig. 13a). It is unclear how extension is consistent with the other observed structures in the region if there is one major stress field, unless this fault marks an extensional basin within the northern block that is not visible in this image. Therefore, multiple stress fields may have been in effect at different times, in which extension was preceded by shortening and dextral motion within the block. The block may also be responding to deeper, pre-existing structures or crustal differences that are not visible at the surface. This could mean that extension could be so localized that it is only happening in one more-or-less isolated area.

4.2.4. Structure of Zal Montes

Zal Montes and Patera display even further the diversity of surface features on Io. Located at 33.7°N, 81.9°W, the Zal region contains two morphologically distinct mountains, designated North and South Zal Mons, with Zal Patera (120 km × 197 km) lying just east of North Zal Mons (~2 km high) and North of South Zal Mons (7.4 km high; Schenk et al., 2001). Additionally, Rustam Patera, a small lava-covered depression, occurs just to the west of South Zal Mons (Bunte et al., 2008; Fig. 14).

Even visually, the two mountains of the Zal region are very different from each other (Fig. 14). North Zal Mons is a nearly flat, smooth plateau, with straight margins that, although scalloped by erosion, are still quite linear. The plateau is ~250 km long and stands about ~2 km above the surrounding plains (Schenk et al., 2001). South Zal Mons, however, has more broadly arcuate boundaries and a lineated, rugged top surface with a narrow ridge crest towards its southern end, more typical of other Ionian mountains. In addition to morphological variation, the long axes of these two mountains are roughly perpendicular to one another (Fig. 14). These contrasting features and orientations argue that major differences exist between the two locations. It is possible that each part formed at a different time under a different stress regime, or that different orientations of basement faults caused the surface to deform differently during regional contraction. This could be further complicated by localized differences in crustal properties or in the nature of volcanism, which, when combined with tectonic stresses, could produce widely different morphologies at the surface.

North Zal Mons does not seem to have experienced the same styles of crustal deformation as those experienced at South Zal Mons or, for that matter, the other mountains described above. North Zal Mons has been fractured on its southern side, but this is likely due to extension and gravitational slumping in concert with larger-scale extensional faults that bound its southern side (Fig. 14). In fact, we have interpreted all of the major boundaries of North Zal Mons as normal faults, due to both their straight natures and to the fact that we see no evidence of crustal shortening on the plateau. There may have been later minor reverse faulting

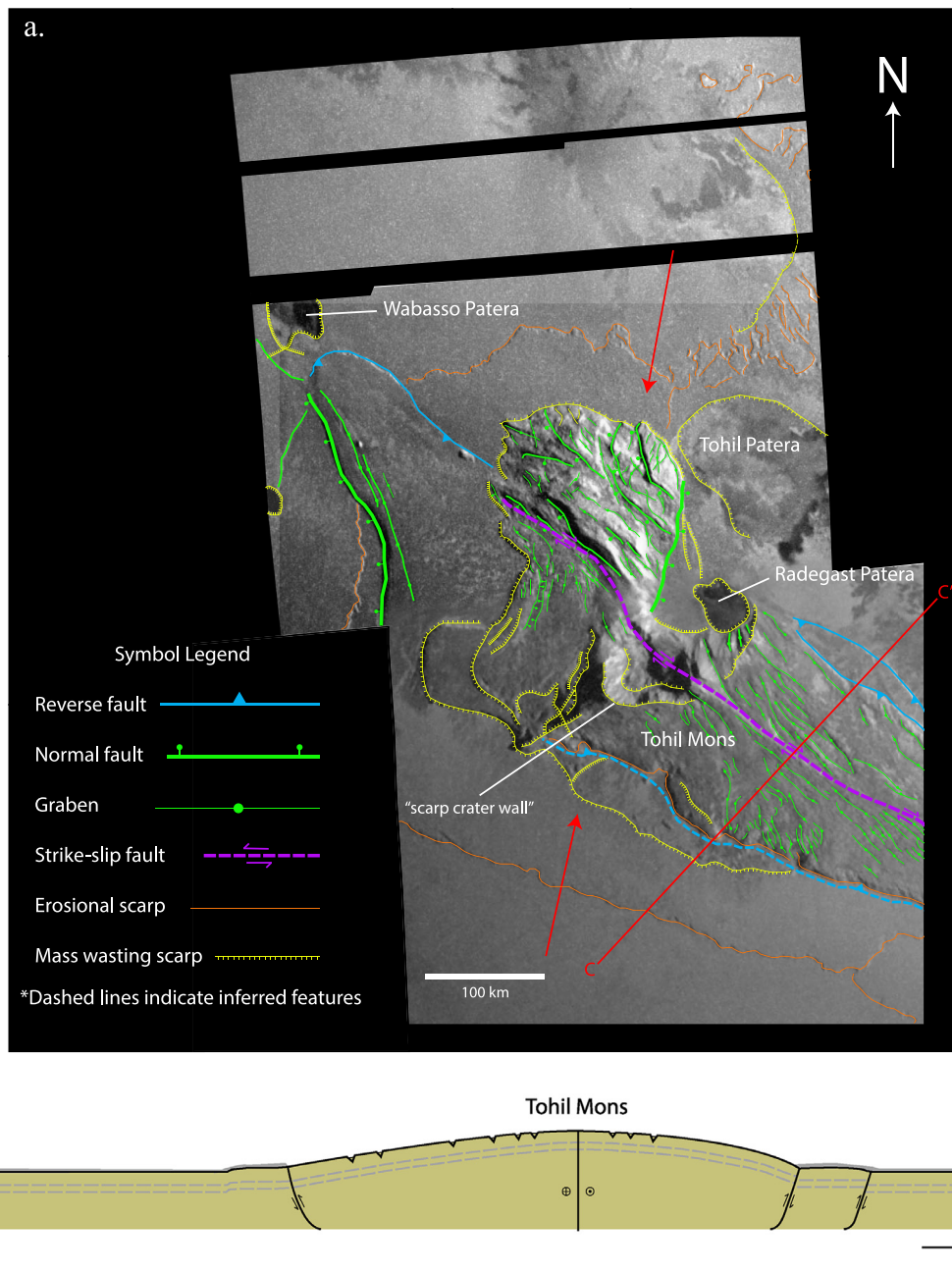


Fig. 13. Tohil Region (28°S, 161°W). (a) Galileo image mosaic (~327 m/pixel) of Tohil Mons, overlain by structural interpretations (previous page). Images were obtained in October 2001. Illumination from the upper right (northeast). The red arrows indicate proposed orientations of principal horizontal stresses, σ_1 (above). (b) Cross section from C to C' (below) as indicated in (a) across Tohil Mons. No vertical axis is specified but vertical exaggeration is about 5x. (For interpretation of the references to colour in this figure legend, the reader is referred to the web version of this article.)

south of North Zal Mons as evidenced by faint, arcuate features in the plain to the south which we interpret to be the surface expression of thrust faults, but these do not seem to interact with or cause any deformation to North Zal Mons itself (Fig. 14). North Zal Mons may be a remnant of older, more resistant crust separated from surrounding volcanic plains by slip along normal faults. This seems the most likely possibility given the morphology and geometry of North Zal Mons and the tectonically formed lineations on and around it.

South Zal Mons, however, shows evidence of horizontal shortening as it has built up steep, tall sides along fairly arcuate boundaries. We interpret these as high-angle reverse faults such as those seen elsewhere on Io. The basin on the west of South Zal Mons that causes its asymmetrical shape may have formed by

right-lateral strike slip faulting that has moved the two halves of the mountain apart to form the intervening basin. As this space opened, blocks on South Zal Mons' steep western side slumped towards the west. The strike-slip motion that has moved the eastern half of South Zal Mons to the south may be the cause of the rather abrupt western face adjacent to the transtensional basin.

The volcanic activity in the area is structurally controlled. Rustam Patera lies along a block-bounding oblique-slip fault that may have opened the transtensional basin it currently resides in on the western side of South Zal Mons (Fig. 14). Additionally, fresh flows on the floor of Zal Patera line up with the bounding normal faults of North Zal Mons. This further shows how fractures and faults in Io's crust serve as magma conduits.

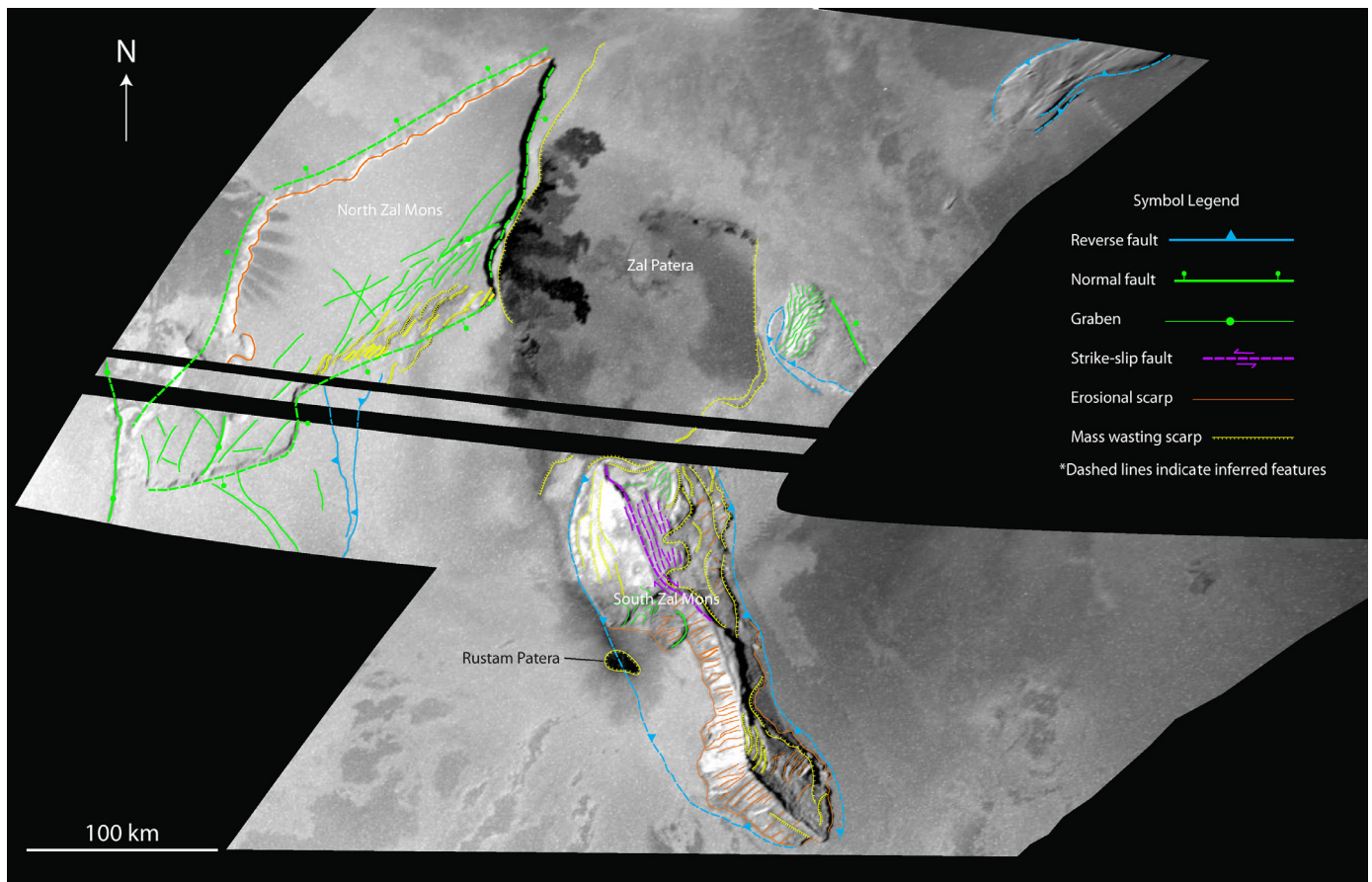


Fig. 14. Zal Region (33.7°N, 81.9°W). Reprojected Galileo images (~260 m/pixel) of the Zal Montes complex, with structural interpretations. Images were obtained November 26, 1999 and February 22, 2000. Illumination from the left (west).

Although Bunte et al. (2008) proposed that the two mountains of Zal were once joined together and subsequently separated through strike-slip motion and transtensional rifting, we do not see geomorphic or tectonic evidence that conclusively supports the hypothesis that they were once a single structure. There appears to have been little to no crustal shortening to the north, given the straight margins of North Zal Mons and the set of sub parallel grabens on the plateau. However, South Zal Mons is an entirely different and complex structure that was involved in significant crustal shortening, accompanied by faulting and tilting or folding during uplift. Moreover, on the undistorted, reprojected images used in this study, the different blocks that were joined together by Bunte et al. (2008) no longer appear to fit. Instead, we propose that North and South Zal Montes never were one mountain but rather that they formed independently. They may be separated by block-bounding faults buried beneath Zal Patera. Nonetheless, this area is challenging to understand; the visible structures can be interpreted in multiple ways, and much of the possibly telling structural features are buried under smooth volcanic plains. We present an alternative hypothesis; yet we recognize that there are strengths and weaknesses to any model since data for the Zal region are limited.

5. Discussion

We propose that Io's mountains result from multiple stress inputs through global and local-scale processes. Over time, relatively uniform global resurfacing by volcanism could generate compressive stress in the crust sufficient to produce local uplift of large, coherent crustal blocks bounded by deep-rooted, high-angle reverse

faults (Schenk and Bulmer, 1998). This would explain the isolated nature of Io's mountains and the fact that we did not observe significant clustering of mountains, but rather clustering of tectonic lineations around mountain complexes. Mountain and adjacent basin formation may be similar to basement-cored, thick-skinned contractional features found on Earth, such as the Laramide-style mountains of the western interior of Utah, Wyoming, Colorado, and New Mexico, USA (Fig. 15; Wise, 1963; Palmquist, 1978).

Fig. 15 shows the relationship of basement uplift along steep reverse faults and gravity sliding. Arching from uplift has led to the formation of keystone grabens in many locations across Io, such as those associated with Hi' iaka Montes, Shamshu Mons, Nemea Planum, or Mongibello Mons. During subsequent extensional faulting and changes in maximum stress, gravitational collapse has freed weaker layers on the major fault-bounded edges of the uplifted blocks.

Although subsidence resulting from global resurfacing is likely the main player in global crustal stress on Io, it is also possible that variable stresses produced by tidal massaging are an additional factor. The significant lack of structural lineations between 75°–100° and 165°–180° identified on a global scale in this study points to control by a global tectonic system with fairly consistent stress orientations. Lateral compression of Io's crust may be a result of diurnal tidal stress fields. The fact that the greatest concentrations of structure orientations are 90° apart from each other could indicate one maximum stress direction, σ_1 , and one direction of least stress, σ_3 . However, the spread of lineation orientations could also indicate changing global stress fields with different σ_1 occurring at different times. Stresses from tidal forces vary diurnally, as well as on larger timescales as a result of the slightly non-synchronous

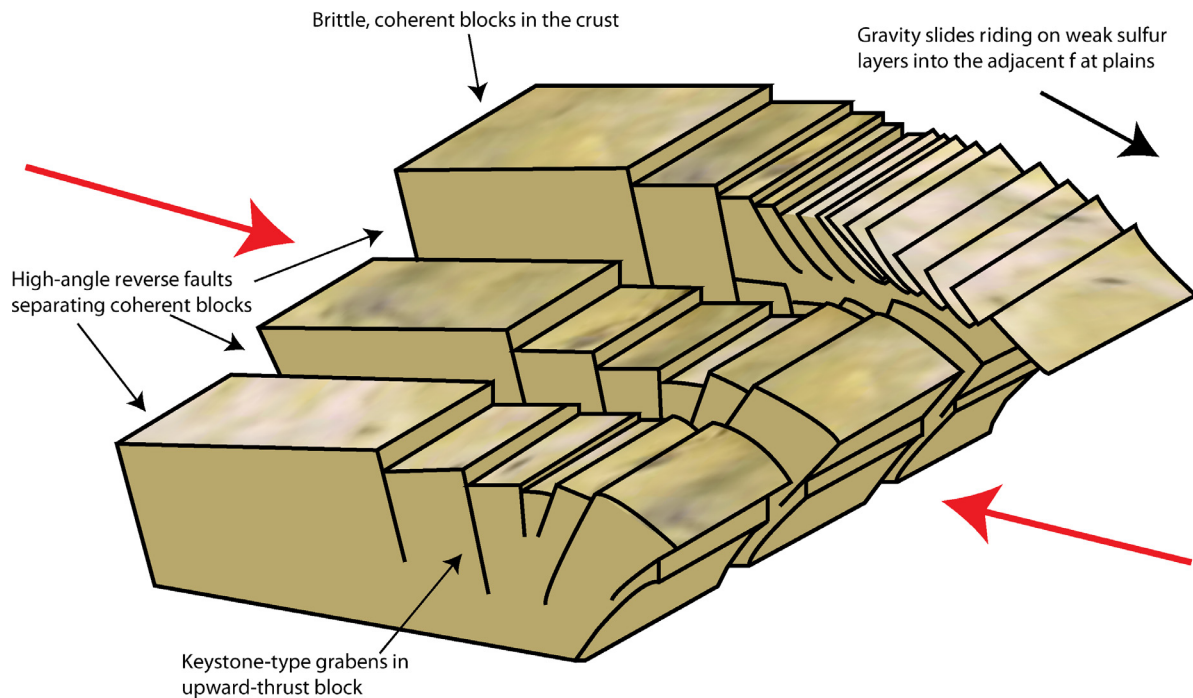


Fig. 15. Generalized block diagram of the formation and evolution of many of Io's mountains, based on Laramide-style basement-cored uplifts seen in much of the western interior of the United States. The red arrows indicate theoretical orientations of principal horizontal stresses, σ_1 . Modified from Wise (1963). (For interpretation of the references to colour in this figure legend, the reader is referred to the web version of this article.)

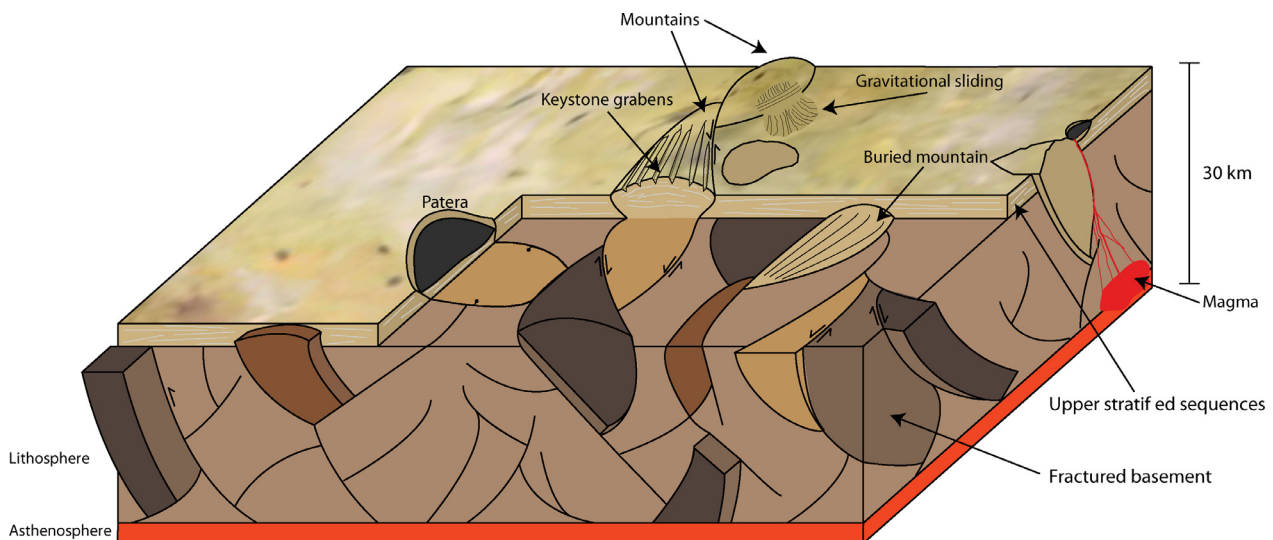


Fig. 16. Generalized block diagram of the basement fault model presented in this study. From global stress inputs such as volcanic loading and tidal forces, stresses oblique to pre-existing basement faults create transtensional openings, transpressional folding, and reverse and normal faulting.

rotation of Io (Yoder, 1979; Yoder and Peale, 1981). Additionally, maximum stress orientations vary by location (Bart et al., 2004). In equatorial regions, predicted maximum stresses are virtually equal in both the north-south and east-west directions and these stresses become increasingly oblique towards the poles. Stresses also vary with longitude as the tidal bulge stretches toward Jupiter and then relaxes throughout an Io day while lagging slightly behind the rotation rate of the moon as a whole (Bart et al., 2004). It is likely that the observed orientations of structural features are a product of diurnally varying tidal stresses.

While mountain formation originates from global processes, our study shows that the regional tectonic and morphologic details are governed by pre-existing local structures in the crust (Fig. 16).

Throughout geologic time and through consistent global stress by global volcanic resurfacing (Schenk and Bulmer, 1998) and tidal flexing, fractures and faults have built up in the crust and have subsequently been buried by successive episodes of volcanism. Then, as stresses continued to be applied, basement faults were reactivated, many by stresses oblique to those that originally formed the faults. This geometry produced oblique strike-slip motion and initiated formation of transtensional and transpressional features along these faults. Transtensional basins opened to allow for thinning of the crust and possible patera formation or magma migration along structures. Crustal blocks continued to move in various directions depending on the orientations of maximum horizontal stress and of basement faults. This explains the seemingly

random orientations, locations, shapes, and sizes of mountains on Io revealed by our statistical study. Geomorphic identification and structural mapping showed that some mountains gently arch while others are more polygonal and straight. At least a few are bounded by straight faults with dominantly normal offsets, others by broadly arcuate, high-angle reverse faults. Mountains on Io represent a combined effect of global and regional tectonic processes, and all have been modified by sapping of volatiles and mass wasting and gravitational collapse of over-steepened slopes. These local-scale processes can be seen virtually everywhere a feature with topographic relief appears on Io.

Deformation on Io is probably thick-skinned rather than thin-skinned because of the very nature of its crust. The crust is most likely dominated by volcanic and intrusive rocks of mafic and ultramafic compositions (McEwen et al., 1989; Carr et al., 1998; Geissler et al., 1999; McEwen et al., 1998; McEwen et al., 2000; Radebaugh et al., 2004). Io's high heat flow probably leads to recrystallization and metamorphism of these mafic protoliths, even at shallow depths, creating a strong "crystalline basement" akin to that of Earth's continents, which is then overlain with thin coverings of volcanic material. Therefore, we conclude that Io's crust is broken into large, coherent blocks with deep, high-angle reverse faults such as those in Laramide-type mountains (Fig. 15; Brewer et al., 1982; Bland and McKinnon, 2016), rather than highly folded and wrinkled by short wavelength folds as found in thin-skinned orogenic belts dominated by thick sequences of layered sedimentary rocks. Recurrent stresses from tidal forces and global volcanic loading throughout Io's existence have driven the formation of these reverse faults and mountains, while also exploiting and re-activating buried structures in continued deformation of Io's crust.

The Laramide Orogeny and its associated thick-skinned tectonic regime resulted from shallow subduction causing stress to accumulate in the base of the crust (Brewer et al., 1982). Similar stresses may be generated on Io, not from subduction of tectonic plates, but from deep, internal tidal stresses or from consistent burial and shortening of the crust by volcanic loading. However these stresses are generated, all would result in a thick-skinned style of crustal deformation (Schenk and Bulmer, 1998; Schenk et al., 2001; Jaeger et al., 2003; Bland and McKinnon, 2016; McGovern et al., 2016).

6. Conclusions

Io provides insight into tectonic features on other planets and moons since there are so many unique landforms available for study. Therefore, a greater understanding of Ionian tectonics and lithospheric properties is key to our knowledge of the workings of tectonics on other bodies in the solar system. The way volcanic and tectonic processes interact on Io can also inform similar processes on other tidally heated bodies both within and beyond the solar system.

Io has some of the tallest and steepest mountains in the solar system and they are uniquely shaped as islands amidst smooth, continually resurfaced plains. They appear to be blocks of older, highly fractured crust, uplifted and modified by both global and local tectonic processes. Movement of the crustal blocks in relation to each other may be governed by the stresses imposed on a brittle crust by tidal massaging and volcanic loading. The morphology of and statistical results describing topographic features suggest that the mountains on Io have been formed under multiple stress regimes. We assume that stress regimes have varied throughout Io's existence in this highly dynamic setting, leaving the crust broken by faults with many orientations. Such pervasive fracturing has enabled the formation of paterae and mountains, which bear unique relationships to each other in distribution and shape.

One mechanism for mountain formation on Earth is that of delamination, in which the lowermost parts of the lithosphere sink

into the asthenosphere. This can happen when mafic (plagioclase-bearing) rocks convert into denser eclogites (where garnet replaces plagioclase) and the lower lithosphere becomes denser than the asthenosphere below it (Bird, 1979; Meissner and Mooney, 1998). Currently, evidence suggests that this is happening beneath the Tibetan Plateau as a result of the collision of India and Asia (Meissner and Mooney, 1998). Since high resurfacing and corresponding mountain uplift rates and frequent mafic to ultramafic volcanism take place on Io, it is possible that delamination of the lithosphere and the associated vertical stresses is a contributing cause of Ionian mountain formation. However, on Io, such transitions would require greater pressures, and therefore greater depths, where temperatures would probably not be hot enough for crustal melting. Thus, Io's steep thermal gradient may prevent complete delamination. At this point we can conclude that Io's lithosphere is sufficiently thick and strong to support mountains, such as Boösaule, as high as 17–18 km in elevation (Schenk et al., 2001), given its compositional and buoyancy constraints.

These statistical and structural studies have increased our understanding of Io's paterae and mountains. But ultimately, to find out how they formed will require higher-resolution images over a greater portion of Io's surface. Even with the benefits of increased resolution, the high rate of resurfacing from volcanic eruptions may continue to keep Io's tectonic histories shrouded from view.

Acknowledgements

We are grateful to the Rocky Mountain NASA Space Grant Consortium for helping to fund this project and for the helpful reviews of Zibi Turtle and Michelle Kirchoff.

References

- Baddeley, A., Turner, R., 2005. Spatstat: an R package for analyzing spatial point patterns. *J. Stat. Software* 12 (6), 1–42.
- Bart, G.D., et al., 2004. Ridges and tidal stress on Io. *Icarus* 169, 111–126.
- Barth, B., Radebaugh, J., 2010. Distribution and comparison of Io's paterae: Effective diameters and active volcanism. *LPSC XLI Abstract* 2666.
- Batschelet, E., et al., 1973. Angular-linear correlation coefficient for rhythometry and circannually changing human birth rates at different geographic latitudes. *Int. J. Chronobiol.* 1, 183–202.
- Bird, P., 1979. Continental delamination and the Colorado Plateau. *J. Geophys. Res.* 84 (B13), 7561–7571.
- Bland, M.T., McKinnon, W.B., 2016. Mountain building on Io driven by deep faulting. *Nature Geosci.* 9, 429–432.
- Blaney, D.L., et al., 1995. Volcanic eruptions on Io: Heat flow, resurfacing, and lava composition. *Icarus* 113, 220–225.
- Brewer, J.A., et al., 1982. COCORP profiling across the Rocky Mountain Front in southern Wyoming, part 1: Laramide structure. *GSA Bull.* 93, 1242–1252.
- Bunte, M.K., Williams, D.A., Greeley, R., 2008. Geologic mapping of the Zal region of Io. *Icarus* 197, 354–367.
- Bunte, M.K., et al., 2010. Geologic mapping of the Hi'iaka and Shamshu regions of Io. *Icarus* 207, 868–886.
- Carr, M.H., et al., 1979. Volcanic features of Io. *Nature* 280, 729–733.
- Carr, M.H., et al., 1998. Mountains and calderas on Io: Possible implications for lithosphere structure and magma generation. *Icarus* 135, 146–165.
- Davies, A., 2001. Volcanism on Io: The view from Galileo. *Astron. Geophys.* 42 (2), 10–2.15.
- Dickinson, W.R., Snyder, W.S., 1978. Plate tectonics of the Laramide orogeny. *GSA Memoirs* 151, 355–366.
- Diggle, P.J., 2013. *Statistical Analysis of Spatio-Temporal Point Patterns*. CRC Press, Oxford, UK.
- Geissler, P.E., et al., 1999. Global color variations on Io. *Icarus* 140, 265–282.
- Gelfand, A.E., et al., 2010. *Handbook of Spatial Statistics*. CRC Press, Oxford, UK.
- Hamilton, C.W., et al., 2013. Spatial distribution of volcanoes on Io: Implications for tidal heating and magma ascent. *Earth Planet. Sci. Lett.* 301, 272–286.
- Hare, T., et al., 2013. Map projection on the web (POW). *LPSC XLIV Abstract* 2068.
- Jaeger, W.L., et al., 2003. Orogenic tectonism on Io. *J. Geophys. Res.* 108 12-1–12-18.
- Johnson, R.A., Wehrly, T., 1977. Measures and models for angular correlation and angular-linear correlation. *Jour. Royal Stat. Soc. Series B* 39, 222–229.
- Johnson, T.V., et al., 1979. Volcanic resurfacing rates and implications for volatiles on Io. *Nature* 280, 746–750.
- Jozwiak, L.M., 2014. Constraining the lithospheric thickness of Io from a modified heat-pipe Model. *LPSC XLV Abstract* 1160.
- Kargel, J.S., Delmelle, P., Nash, D.B., 1999. Volcanogenic sulfur on Earth and Io: composition and spectroscopy. *Icarus* 142, 249–280.

- Keszthelyi, L., McEwen, A., 1997. Magmatic differentiation of Io. *Icarus* 130, 437–448.
- Keszthelyi, L.P., McEwen, A.F., Taylor, G.J., 1999. Revisiting the hypothesis of a mushy magma ocean in Io. *Icarus* 141, 415–419.
- Keszthelyi, L.P., et al., 2004. A post-Galileo view of Io's interior. *Icarus* 169, 271–286.
- Kirchoff, M.R., McKinnon, W.B., 2009. Formation of mountains on Io: variable volcanism and thermal stresses. *Icarus* 201, 598–614.
- Kirchoff, M.R., McKinnon, W.B., Schenk, P., 2011. Global distribution of volcanic centers and mountains on Io: Control by asthenospheric heating and implications for mountain formation. *Earth Planet. Sci. Lett.* 301, 22–30.
- Leone, G., Wilson, L., Davies, A.G., 2011. The geothermal gradient of Io: Consequences for lithosphere structure and volcanic activity. *Icarus* 211, 623–635.
- Lopes-Gautier, R.M., et al., 1999. Active volcanism on Io: global distribution and variations in activity. *Icarus* 140, 243–264.
- Lopes, R.M.C., et al., 2004. Lava lakes on Io: Observations of Io's volcanic activity from Galileo NIMS during the 2001 fly-bys. *Icarus* 169, 140–174.
- Lopes, R.M.C., Williams, D.A., 2005. Io after Galileo. *Rep. Prog. Phys.* 68, 303–340.
- Lowry, R., 2015. Wilcoxon signed-rank test. Concepts and applications of inferential statistics. <http://vassarstats.net/textbook/ch12a.html> (accessed 8.5.16).
- Mann, P., 2007. Global catalogue, classification, and tectonic origins of restraining- and releasing bends on active and ancient strike-slip fault systems. *Geol. Soc. of Lon. Spec. Pub.* 290, 13–142.
- McEwen, A.S., Soderblom, L.A., 1983. Two classes of volcanic plumes on Io. *Icarus* 55, 191–217.
- McEwen, A.S., et al., 1985. Volcanic hot spots on Io: Correlation with low-albedo calderas. *J. Geophys. Res.* 90, 12345–12379.
- McEwen, A.S., Lunine, J., Carr, M.H., 1989. Dynamic geophysics of Io. Time-Variable Phenomena in the Jovian System, NASA Spec. Pub., NASASP-464, 11–47.
- McEwen, A.S., et al., 1998. High-temperature silicate volcanism on Jupiter's moon Io. *Science* 281 (5373), 87–90.
- McEwen, A.S., et al., 2000. Galileo at Io: Results from High-Resolution Imaging. *Science* 288, 1193–1198.
- McGovern, P.J., et al., 2016. Magma ascent pathways associated with large mountains on Io. *Icarus* 272, 246–257.
- McKinnon, W.B., Schenk, P.M., Dombard, A.J., 2001. Chaos on Io: A model for formation of mountain blocks by crustal heating, melting, and tilting. *Geology* 29, 103–106.
- Meissner, R., Mooney, W., 1998. Weakness of the lower continental crust: A condition for delamination, uplift, and escape. *Tectonophysics* 296 (1), 47–60.
- Moore, W.B., 2001. The thermal state of Io. *Icarus* 154 (2), 548–550.
- Morabito, L.A., et al., 1979. Discovery of currently active extraterrestrial volcanism. *Science* 204, 972.
- Nash, D.B., et al., 1986. Io. *Satellites*. University of Arizona, Tucson, pp. 629–688.
- O'Reilly, T.C., Davies, G.F., 1981. Magma transport of heat on Io: a mechanism allowing a thick lithosphere. *Geophys. Res. Lett.* 8, 313–316. doi:10.1029/GL008i004p00313.
- Palmquist, J.C., 1978. Laramide structures and basement block faulting: Two examples from the Big Horn Mountains, Wyoming. *GSA Memoirs*, 151, 125–138.
- Peale, S.J., Cassen, P., Reynolds, R.T., 1979. Melting of Io by tidal dissipation. *Science* 203, 892–894.
- R Core Team, 2015. R: A language and environment for statistical computing. R Foundation for Statistical Computing, Vienna. URL: <http://www.R-project.org/>.
- Radebaugh, J., et al., 2001. Paterae on Io: A new type of volcanic caldera? *J. Geophys. Res.* 106 (33), 005–033 020.
- Radebaugh, J., et al., 2004. Observations and temperatures of Io's Pele Patera from Cassini and Galileo spacecraft images. *Icarus* 169, 65–79.
- Radebaugh, J., 2005. Formation and evolution of paterae on Jupiter's moon Io. Doctoral Dissertation. University of Arizona, Tucson.
- Radebaugh, J., Schleiffarth, K., Christiansen, E.H., 2011. Internal stresses of Io are revealed by surface lineations. LPSC XVII. Abstract 2755.
- Rathbun, J., et al., 2002. Loki, Io: A periodic volcano. *Geophys. Res. Lett.* 29, 84–1–84–4.
- Ross, M.N., et al., 1990. Internal structure of Io and the global distribution of its topography. *Icarus* 85, 309–325.
- Sagan, C., 1979. Sulphur flows on Io. *Nature* 280, 750–753.
- Schaber, G.G., 1982. *The Satellites of Jupiter*. University of Arizona, Tucson, pp. 556–597.
- Schenk, P.M., Bulmer, M.H., 1998. Origin of mountains on Io by thrust faulting and large-scale mass movements. *Science* 6, 1514–1517.
- Schenk, P.M., Hargitai, H., 1998. Morphology and distribution of mountains on Io. *Bull. Am. Astro. Soc.* 30 Abstract 1121.
- Schenk, P., et al., 2001. The mountains of Io: Global and geological perspectives from Voyager and Galileo. *J. Geophys. Res.* 106 (33), 201–233 222.
- Segatz, M., et al., 1988. Tidal dissipation, surface heat flow, and figure of viscoelastic models of Io. *Icarus* 75, 187–206.
- Smith, B.A., et al., 1979. The Jupiter system through the eyes of Voyager I. *Science* 204, 951–972.
- Spencer, J.R., et al., 2007. Io volcanism seen by New Horizons: a major eruption of the Tvashtar volcano. *Science* 318, 240–243.
- Spotila, J.A., Farley, K.A., Sieh, K., 1998. Uplift and erosion of the San Bernardino Mountains associated with transpression along the San Andreas Fault, California, as constrained by radiogenic helium thermochronometry. *Tectonics* 17, 360–378.
- Strom, R.G., et al., 1979. Volcanic eruption plumes on Io. *Nature* 280, 733–736.
- Tackley, P.J., et al., 2001. Three-dimensional simulations of mantle convection in Io. *Icarus* 149, 79–93.
- Tasdan, F., Cetin, M., 2013. A simulation study on the influence of ties on uniform scores test for circular data. *Jour. Appl. Stat.* 41, 1137–1146.
- Tu, R., 2015. A study of the parametric and nonparametric linear-circular correlation coefficient. California Polytechnic State University, San Luis Obispo, 1–2.
- Turcotte, D.L., Schubert, G., 2002. *Geodynamics*, 2nd ed. Cambridge, Cambridge, UK, 456.
- Turtle, E.P., et al., 2001. Mountains on Io: High-resolution Galileo observations, initial interpretations, and formation models. *J. Geophys. Res.* 106, 33175–33199.
- Turtle, E.P., Jaeger, W.L., Schenk, P., 2007. *Io After Galileo*. Springer/Praxis, Chichester, UK, pp. 109–131.
- Veeder, G.J., et al., 1994. Io's heat flow from infrared radiometry: 1983–1993. *J. Geophys. Res.* 99, 17095–17162.
- Veeder, G.J., et al., 2004. The polar contribution to the heat flow of Io. *Icarus* 169, 264–270.
- Veeder, G.J., et al., 2009. Io: Heat flow from dark volcanic fields. *Icarus* 204, 239–253.
- Veeder, G.J., et al., 2011. Io: Heat flow from dark paterae. *Icarus* 212, 236–261.
- Williams, D.A., et al., 2002. Geologic mapping of the Chaac-Camaxtli region of Io from Galileo imaging data. *J. Geophys. Res.* 107, 6.1–6.13.
- Williams, D., et al., 2004. Mapping of the Culann-Tohil region of Io from Galileo imaging data. *Icarus* 169, 80–97.
- Williams, D.A., Howell, R., 2007. *Io After Galileo*. Springer/Praxis, Chichester, UK, pp. 133–161.
- Williams, D., et al., 2012. Geologic Map of Io, U.S. Geological Survey Scientific Investigations, Map 3168, scale 1:15,000,000.
- Wise, D.C., 1963. Keystone faulting and gravity sliding driven by basement uplift of Owl Creek Mountains, Wyoming. *AAPG Bull.* 47, 586–598.
- Yoder, C.F., 1979. How tidal heating in Io drives the Galilean orbital resonance locks. *Nature* 279, 767–770.
- Yoder, C.F., Peale, S.J., 1981. The tides of Io. *Icarus* 47, 1–35.
- Zhang, Q., et al., 2002. Investigation of the distribution and characteristics of Ionian paterae using a relational database. LPSC XXXIII. Abstract 1137.